

Measurement of the branching ratio of ^{16}N , ^{15}C , ^{12}B , and ^{13}B isotopes through the nuclear muon capture reaction in the Super-Kamiokande detector

Y. Maekawa,²⁴ K. Abe,^{1, 49} S. Abe,¹ Y. Asaoka,^{1, 49} M. Harada,¹ Y. Hayato,^{1, 49} K. Hiraide,^{1, 49} K. Hosokawa,¹ K. Ieki,^{1, 49} M. Ikeda,^{1, 49} J. Kameda,^{1, 49} Y. Kanemura,¹ Y. Kataoka,^{1, 49} S. Miki,¹ S. Mine,^{1, 7} M. Miura,^{1, 49} S. Moriyama,^{1, 49} M. Nakahata,^{1, 49} S. Nakayama,^{1, 49} Y. Noguchi,¹ G. Pronost,¹ K. Sato,¹ H. Sekiya,^{1, 49} K. Shimizu,¹ R. Shinoda,¹ M. Shiozawa,^{1, 49} Y. Suzuki,¹ A. Takeda,^{1, 49} Y. Takemoto,^{1, 49} H. Tanaka,^{1, 49} T. Yano,¹ Y. Itow,^{2, 32, 33} T. Kajita,^{2, 49, 23} R. Nishijima,² K. Okumura,^{2, 49} T. Tashiro,² T. Tomiya,² X. Wang,² P. Fernandez,³ L. Labarga,³ D. Samudio,³ B. Zaldivar,³ C. Yanagisawa,^{4, 36} E. Kearns,^{5, 49} J. Mirabito,⁵ L. Wan,⁵ T. Wester,⁵ B. W. Pointon,^{6, 53} J. Bian,⁷ B. Cortez,⁷ N. J. Grishevich,⁷ Y. Jiang,⁷ M. B. Smy,^{7, 49} H. W. Sobel,^{7, 49} V. Takhistov,^{7, 25} A. Yankelevich,⁷ J. Hill,⁸ M. C. Jang,⁹ S. H. Lee,⁹ D. H. Moon,⁹ R. G. Park,⁹ B. S. Yang,⁹ B. Bodur,¹⁰ K. Scholberg,^{10, 49} C. W. Walter,^{10, 49} A. Beauchêne,¹¹ O. Drapier,¹¹ A. Ershova,¹¹ Th. A. Mueller,¹¹ A. D. Santos,¹¹ P. Paganini,¹¹ C. Quach,¹¹ R. Rogly,¹¹ T. Nakamura,¹² J. S. Jang,¹³ R. P. Litchfield,¹⁴ L. N. Machado,¹⁴ F. J. P. Soler,¹⁴ J. G. Learned,¹⁵ K. Choi,¹⁶ N. Iovine,¹⁶ S. Cao,¹⁷ L. H. V. Anthony,¹⁸ D. Martin,¹⁸ N. W. Prouse,¹⁸ M. Scott,¹⁸ Y. Uchida,¹⁸ V. Berardi,¹⁹ N. F. Calabria,¹⁹ M. G. Catanesi,¹⁹ N. Ospina,¹⁹ E. Radicioni,¹⁹ A. Langella,²⁰ G. De Rosa,²⁰ G. Collazuol,²¹ M. Feltre,²¹ M. Mattiazzi,²¹ L. Ludovici,²² M. Gonin,²³ L. Périssé,²³ B. Quilain,²³ S. Horiuchi,²⁴ A. Kawabata,²⁴ M. Kobayashi,²⁴ Y. M. Liu,²⁴ Y. Nishimura,²⁴ R. Okazaki,²⁴ R. Akutsu,²⁵ M. Friend,²⁵ T. Hasegawa,²⁵ Y. Hino,²⁵ T. Ishida,²⁵ T. Kobayashi,²⁵ M. Jakkapu,²⁵ T. Matsubara,²⁵ T. Nakadaira,²⁵ K. Nakamura,^{25, 49} Y. Oyama,²⁵ A. Portocarrero Yrey,²⁵ K. Sakashita,²⁵ T. Sekiguchi,²⁵ T. Tsukamoto,²⁵ N. Bhuiyan,²⁶ G. T. Burton,²⁶ R. Kralik,²⁶ N. Latham,²⁶ F. Di Lodovico,²⁶ J. Gao,²⁶ T. Katori,²⁶ J. Migenda,²⁶ R. M. Ramsden,²⁶ Z. Xie,²⁶ S. Zsoldos,^{26, 49} H. Ito,²⁷ T. Sone,²⁷ A. T. Suzuki,²⁷ Y. Takagi,²⁷ Y. Takeuchi,^{27, 49} S. Wada,²⁷ H. Zhong,²⁷ J. Feng,²⁸ L. Feng,²⁸ S. Han,²⁸ J. Hikida,²⁸ J. R. Hu,²⁸ Z. Hu,²⁸ M. Kawaue,²⁸ T. Kikawa,²⁸ T. Nakaya,^{28, 49} T. V. Ngoc,²⁸ R. A. Wendell,^{28, 49} K. Yasutome,²⁸ S. J. Jenkins,²⁹ N. McCauley,²⁹ A. Tarrant,²⁹ M. Fanì,³⁰ M. J. Wilking,³⁰ Z. Xie,³⁰ Y. Fukuda,³¹ H. Menjo,³² Y. Yoshioka,³² J. Lagoda,³⁴ M. Mandal,³⁴ Y. S. Prabhu,³⁴ J. Zalipska,³⁴ M. Mori,³⁵ M. Jia,³⁶ J. Jiang,³⁶ W. Shi,³⁶ K. Hamaguchi,³⁷ H. Ishino,³⁷ Y. Koshio,^{37, 49} F. Nakanishi,³⁷ S. Sakai,³⁷ T. Tada,³⁷ T. Tano,³⁷ T. Ishizuka,³⁸ G. Barr,³⁹ D. Barrow,³⁹ L. Cook,^{39, 49} S. Samani,³⁹ D. Wark,^{39, 45} A. Holin,⁴⁰ F. Nova,⁴⁰ S. Jung,⁴¹ J. Y. Yang,⁴¹ J. Yoo,⁴¹ J. E. P. Fannon,⁴² L. Kneale,⁴² M. Malek,⁴² J. M. McElwee,⁴² T. Peacock,⁴² P. Stowell,⁴² M. D. Thiesse,⁴² L. F. Thompson,⁴² S. T. Wilson,⁴² H. Okazawa,⁴³ S. M. Lakshmi,⁴⁴ E. Kwon,⁴⁶ M. W. Lee,⁴⁶ J. W. Seo,⁴⁶ I. Yu,⁴⁶ A. K. Ichikawa,⁴⁷ K. D. Nakamura,⁴⁷ S. Tairafune,⁴⁷ A. Eguchi,⁴⁸ S. Goto,⁴⁸ H. Hayasaki,⁴⁸ S. Kodama,⁴⁸ Y. Masaki,⁴⁸ Y. Mizuno,⁴⁸ T. Muro,⁴⁸ K. Nakagiri,⁴⁸ Y. Nakajima,^{48, 49} N. Taniuchi,⁴⁸ E. Watanabe,⁴⁸ M. Yokoyama,^{48, 49} P. de Perio,⁴⁹ S. Fujita,⁴⁹ C. Jesús-Valls,⁴⁹ K. Martens,⁴⁹ Ll. Martí,⁴⁹ K. M. Tsui,⁴⁹ M. R. Vagins,^{49, 7} J. Xia,⁴⁹ S. Izumiyama,⁵⁰ M. Kuze,⁵⁰ R. Matsumoto,⁵⁰ K. Terada,⁵⁰ R. Asaka,⁵¹ M. Ishitsuka,⁵¹ M. Shinoki,⁵¹ M. Sugo,⁵¹ M. Wako,⁵¹ K. Yamauchi,⁵¹ T. Yoshida,⁵¹ Y. Nakano,^{52, *} F. Cormier,⁵³ R. Gaur,⁵³ V. Gousy-Leblanc,^{53, †} M. Hartz,⁵³ A. Konaka,⁵³ X. Li,⁵³ B. R. Smithers,⁵³ S. Chen,⁵⁴ Y. Wu,⁵⁴ B. D. Xu,⁵⁴ A. Q. Zhang,⁵⁴ B. Zhang,⁵⁴ M. Girgis,⁵⁵ P. Govindaraj,⁵⁵ M. Posiadala-Zezula,⁵⁵ Y. S. Prabhu,⁵⁵ S. B. Boyd,⁵⁶ R. Edwards,⁵⁶ D. Hadley,⁵⁶ M. Nicholson,⁵⁶ M. O'Flaherty,⁵⁶ B. Richards,⁵⁶ A. Ali,^{57, 53} B. Jamieson,⁵⁷ S. Amanai,⁵⁸ C. Bronner,⁵⁸ D. Horiguchi,⁵⁸ A. Minamino,⁵⁸ Y. Sasaki,⁵⁸ R. Shibayama,⁵⁸ and R. Shimamura⁵⁸

(The Super-Kamiokande Collaboration)

¹Kamioka Observatory, Institute for Cosmic Ray Research, University of Tokyo, Kamioka, Gifu 506-1205, Japan

²Research Center for Cosmic Neutrinos, Institute for Cosmic Ray Research, University of Tokyo, Kashiwa, Chiba 277-8582, Japan

³Department of Theoretical Physics, University Autonoma Madrid, 28049 Madrid, Spain

⁴Science Department, Borough of Manhattan Community College / City University of New York, New York, New York, 1007, USA

⁵Department of Physics, Boston University, Boston, MA 02215, USA

⁶Department of Physics, British Columbia Institute of Technology, Burnaby, BC, V5G 3H2, Canada

⁷Department of Physics and Astronomy, University of California, Irvine, Irvine, CA 92697-4575, USA

⁸Department of Physics, California State University, Dominguez Hills, Carson, CA 90747, USA

⁹Institute for Universe and Elementary Particles, Chonnam National University, Gwangju 61186, Korea

¹⁰Department of Physics, Duke University, Durham NC 27708, USA

¹¹Ecole Polytechnique, IN2P3-CNRS, Laboratoire Leprince-Ringuet, F-91120 Palaiseau, France

¹²Department of Physics, Gifu University, Gifu, Gifu 501-1193, Japan

¹³GIST College, Gwangju Institute of Science and Technology, Gwangju 500-712, Korea

¹⁴School of Physics and Astronomy, University of Glasgow, Glasgow, Scotland, G12 8QQ, United Kingdom

¹⁵Department of Physics and Astronomy, University of Hawaii, Honolulu, HI 96822, USA

¹⁶Center for Underground Physics, Institute for Basic Science (IBS), Daejeon, 34126, Korea
¹⁷Institute For Interdisciplinary Research in Science and Education, ICISE, Quy Nhon, 55121, Vietnam
¹⁸Department of Physics, Imperial College London , London, SW7 2AZ, United Kingdom
¹⁹Dipartimento Interuniversitario di Fisica, INFN Sezione di Bari and Università e Politecnico di Bari, I-70125, Bari, Italy
²⁰Dipartimento di Fisica, INFN Sezione di Napoli and Università di Napoli, I-80126, Napoli, Italy
²¹Dipartimento di Fisica, INFN Sezione di Padova and Università di Padova, I-35131, Padova, Italy
²²INFN Sezione di Roma and Università di Roma “La Sapienza”, I-00185, Roma, Italy
²³ILANCE, CNRS - University of Tokyo International Research Laboratory, Kashiwa, Chiba 277-8582, Japan
²⁴Department of Physics, Keio University, Yokohama, Kanagawa, 223-8522, Japan
²⁵High Energy Accelerator Research Organization (KEK), Tsukuba, Ibaraki 305-0801, Japan
²⁶Department of Physics, King’s College London, London, WC2R 2LS, UK
²⁷Department of Physics, Kobe University, Kobe, Hyogo 657-8501, Japan
²⁸Department of Physics, Kyoto University, Kyoto, Kyoto 606-8502, Japan
²⁹Department of Physics, University of Liverpool, Liverpool, L69 7ZE, United Kingdom
³⁰School of Physics and Astronomy, University of Minnesota, Minneapolis, MN 55455, USA
³¹Department of Physics, Miyagi University of Education, Sendai, Miyagi 980-0845, Japan
³²Institute for Space-Earth Environmental Research, Nagoya University, Nagoya, Aichi 464-8602, Japan
³³Kobayashi-Maskawa Institute for the Origin of Particles and the Universe, Nagoya University, Nagoya, Aichi 464-8602, Japan
³⁴National Centre For Nuclear Research, 02-093 Warsaw, Poland
³⁵National Institute of Technology, Numazu College, Numazu, Shizuoka 410-8501, Japan
³⁶Department of Physics and Astronomy, State University of New York at Stony Brook, NY 11794-3800, USA
³⁷Department of Physics, Okayama University, Okayama, Okayama 700-8530, Japan
³⁸Media Communication Center, Osaka Electro-Communication University, Neyagawa, Osaka, 572-8530, Japan
³⁹Department of Physics, Oxford University, Oxford, OX1 3PU, United Kingdom
⁴⁰Rutherford Appleton Laboratory, Harwell, Oxford, OX11 0QX, UK
⁴¹Department of Physics and Astronomy, Seoul National University, Seoul 151-742, Korea
⁴²School of Mathematical and Physical Sciences, University of Sheffield, S3 7RH, Sheffield, United Kingdom
⁴³Department of Informatics in Social Welfare, Shizuoka University of Welfare, Yaizu, Shizuoka, 425-8611, Japan
⁴⁴August Cieślowski Institute of Physics, University of Silesia in Katowice, 75 Putku Piechoty 1, 41-500 Chorzów, Poland
⁴⁵STFC, Rutherford Appleton Laboratory, Harwell Oxford, and
Daresbury Laboratory, Warrington, OX11 0QX, United Kingdom
⁴⁶Department of Physics, Sungkyunkwan University, Suwon 440-746, Korea
⁴⁷Department of Physics, Faculty of Science, Tohoku University, Sendai, Miyagi, 980-8578, Japan
⁴⁸Department of Physics, University of Tokyo, Bunkyo, Tokyo 113-0033, Japan
⁴⁹Kavli Institute for the Physics and Mathematics of the Universe (WPI), The University of
Tokyo Institutes for Advanced Study, University of Tokyo, Kashiwa, Chiba 277-8583, Japan
⁵⁰Department of Physics, Institute of Science Tokyo, Meguro, Tokyo 152-8551, Japan
⁵¹Department of Physics, Faculty of Science and Technology, Tokyo University of Science, Noda, Chiba 278-8510, Japan
⁵²Faculty of Science, University of Toyama, Toyama City, Toyama 930-8555, Japan
⁵³TRIUMF, 4004 Wesbrook Mall, Vancouver, BC, V6T2A3, Canada
⁵⁴Department of Engineering Physics, Tsinghua University, Beijing, 100084, China
⁵⁵Faculty of Physics, University of Warsaw, Warsaw, 02-093, Poland
⁵⁶Department of Physics, University of Warwick, Coventry, CV4 7AL, UK
⁵⁷Department of Physics, University of Winnipeg, MB R3J 3L8, Canada
⁵⁸Department of Physics, Yokohama National University, Yokohama, Kanagawa, 240-8501, Japan

(Dated: December 10, 2025)

The Super-Kamiokande detector has measured solar neutrinos for more than 25 years. The sensitivity for solar neutrino measurement is limited by the uncertainties of energy scale and background modeling. Decays of unstable isotopes with relatively long half-lives through nuclear muon capture, such as ^{16}N , ^{15}C , ^{12}B and ^{13}B , are detected as background events for solar neutrino observations. In this study, we developed a method to form a pair of stopping muon and decay candidate events and evaluated the production rates of such unstable isotopes. We then measured their branching ratios considering both their production rates and the estimated number of nuclear muon capture processes as $Br(^{16}\text{N}) = (9.0 \pm 0.1)\%$, $Br(^{15}\text{C}) = (0.6 \pm 0.1)\%$, $Br(^{12}\text{B}) = (0.98 \pm 0.18)\%$, $Br(^{13}\text{B}) = (0.14 \pm 0.12)\%$, respectively. The result for ^{16}N has world-leading precision at present and the results for ^{15}C , ^{12}B , and ^{13}B are the first branching ratio measurements for those isotopes.

* Corresponding author: ynakano@sci.u-toyama.ac.jp

† also at University of Victoria, Department of Physics and Astronomy, PO Box 1700 STN CSC, Victoria, BC V8W 2Y2, Canada.

I. INTRODUCTION

A. Solar neutrinos in the Super-Kamiokande

In the last 50 years, solar neutrinos have been measured by several experiments [1–16]. Through solar neutrino measurements by the Super-Kamiokande(SK) and SNO experiments, flavour conversion of solar neutrinos was discovered, leading to the confirmation of neutrino oscillation [6, 7]. The next targets in furthering our understanding of neutrino oscillation are the searches for the matter effect of solar neutrino oscillation, such as the MSW effect in the Sun predicted by Mikheyev, Smirnov, and Wolfenstein [17, 18], and the day/night flux asymmetry induced by the matter effect in the Earth [19–24].

The SK detector has precisely measured the flux of ${}^8\text{B}$ solar neutrinos and its energy spectrum for more than 25 years since 1996 by selecting recoiled electron events via elastic scattering of solar neutrinos [25–29]. By analyzing the Cherenkov light pattern from the recoil electron, the SK detector can reconstruct the time of elastic scattering, as well as the direction and the energy of the scattered electron. These measurements allow us to search for the MSW effect and the day/night flux asymmetry of solar neutrinos. Although the SK detector has already accumulated more than 10^5 solar neutrino interaction events, the sensitivity of SK to the matter effect is primarily limited by the statistics of observed signal, the uncertainty of the energy scale for the recoil electron, as well as the uncertainties on background events, such as radon dissolved in water [30] and spallation products induced by penetrating muons [31, 32]. To reduce the uncertainty on the total amount of background events and to increase sensitivity to solar neutrinos, the uncertainty that comes from the production rates of muon-induced background should be measured.

B. Unstable isotopes by nuclear muon capture process

The negative muon capture rate on nucleons has been studied to theoretically and experimentally understand the nuclear response through the weak interaction [33–38]. Such reactions are used to study nuclear structure and dynamics, where the weak structure at low energies determines weak reaction rates with nuclei.

A negative muon that slows down in the water that fills the SK detector can form a muonic atom with an oxygen through the Coulomb force [39]. The muon in the oxygen’s orbit can then either decay or undergo a muon capture on nuclei [40, 41]. Table I summarizes the branching ratios of unstable isotopes produced by nuclear muon capture process on oxygen. Because a limited number of isotope branching ratios have been measured [40, 42], any further development of the simulation will be insufficient to estimate the branching ratios induced by nuclear muon capture processes in oxygen.

Currently, the expected branching ratios from three simulation codes are available; **Geant4** [43], **Fluka** [44], and **PHITS** [45, 46]. The latter is the Monte Carlo simulation using particle and heavy ions transport with recently developed muon interaction models. Table I summarizes simulated outputs from three simulations. They are inconsistent with each other. Therefore, additional measurements of the branching ratio are required to improve the predictive capability of nuclear muon capture processes in those simulations.

TABLE I. Summary of branching ratios of negative muon capture on oxygen nuclei. A limited number of isotopes have been measured [40, 42]. Some isotopes are not produced based on the simulated values from **PHITS** [45, 46], **Geant4** [43], and **Fluka** (version 4-5.0) [44, 47]. The “Other” row in **Fluka** includes the combination of light particle emissions without any production of residual nuclei listed^a.

Isotope	Measurement data		MC simulation		
	Ref. [42] [%]	Ref. [40] [%]	PHITS [%]	Geant4 [%]	Fluka [%]
${}^{16}\text{N}$	–	11 ± 1	0.5	12.0	5.52
${}^{15}\text{N}$	–	–	57	40.5	61.9
${}^{14}\text{N}$	–	–	21	6.7	2.26
${}^{13}\text{N}$	–	–	0.4	0.1	0.02
${}^{15}\text{C}$	–	–	0.19	0.7	0.67
${}^{14}\text{C}$	13.7 ± 1.1	–	5.14	4.3	3.54
${}^{13}\text{C}$	–	–	5.1	5.5	2.76
${}^{12}\text{C}$	–	–	3.2	2.3	1.24
${}^{11}\text{C}$	–	–	–	0.007	0.046
${}^{14}\text{B}$	–	–	–	0.002	0.002
${}^{13}\text{B}$	–	–	0.02	–	0.088
${}^{12}\text{B}$	–	–	1.16	7.6	4.41
${}^{11}\text{B}$	–	–	5.4	13.6	7.65
${}^{10}\text{B}$	–	–	0.27	1.2	0.87
${}^{11}\text{Be}$	–	–	0.01	0.005	0.037
${}^{10}\text{Be}$	0.43 ± 0.03	–	0.14	0.7	0.91
${}^9\text{Be}$	–	–	0.05	0.7	1.06
${}^7\text{Be}$	0.02 ± 0.01	–	–	0.03	0.15
${}^9\text{Li}$	–	–	–	0.008	0.062
${}^8\text{Li}$	–	–	0.13	1.0	0.52
${}^7\text{Li}$	–	–	0.53	1.9	1.87
${}^6\text{Li}$	–	–	0.05	0.9	1.69
Other	–	–	–	–	2.4

^a Such as $3\alpha + {}^3\text{H} + n$, $3\alpha + {}^2\text{H} + 2n$, and $3\alpha + p + 3n$.

In the SK detector, products of β decays with large Q -values of unstable isotopes can be detected by Cherenkov light. If these unstable isotopes have a relatively long half-life, the decays occur long enough after the muon stops that the two events are separately recorded in the analysis sample. In such a case, the production rates of unstable isotopes by the nuclear muon capture process can be measured by forming a pair of parent-stopping muon and isotope decay candidate events. Table II summarizes the Q -values of β decay and half-lives of four unstable nuclei which can be detected in the SK detector. The ${}^{16}\text{N}$ and ${}^{15}\text{C}$ nuclei have relatively long half-lives

of several seconds and the ^{13}B and ^{12}B nuclei have half-lives of milliseconds. By observing these types of decay events after a stopping muon event is detected, we can evaluate the fraction of isotopes via both decay time and energy distributions and thereby measure the branching ratio of the nuclear muon capture process on oxygen.

TABLE II. Summary of the production reaction, Q -values of β decay, and the half-lives of the unstable isotopes induced by nuclear muon capture. More details are described in Sec. III.

Isotope	Reaction	Q -value of β decay [MeV]	Half-life [s]
^{16}N	$^{16}\text{O}(\mu^-, \nu)^{16}\text{N}$	10.42	7.13
^{15}C	$^{16}\text{O}(\mu^-, \nu p)^{15}\text{C}$	9.77	2.45
^{13}B	$^{16}\text{O}(\mu^-, \nu n 2p)^{13}\text{B}$	13.44	0.0172
^{12}B	$^{16}\text{O}(\mu^-, \nu \alpha)^{12}\text{B}$	13.37	0.0202

This article is organized as follows. In Sec. II, we briefly describe the SK detector, data acquisition system, and energy calibration in the SK experiment. In Sec. III, we give an overview of the decay processes of four unstable isotopes, ^{16}N , ^{15}C , ^{12}B , and ^{13}B , which can be detected in SK, and we also present the theoretical predictions of their production rates at the underground experimental site of the SK detector. In Sec. IV, we describe the analysis methods, which include the selection of stopping muon, the tagging method of ^{16}N and ^{15}C decay candidate events, the χ^2 method to determine the production rates of ^{16}N and ^{15}C , the systematic uncertainties on the measurement, and the measurement result of the production rates of ^{16}N and ^{15}C . In Sec. V, we describe the analysis method and result for the measurement of ^{12}B and ^{13}B production rates. In Sec. VI, we describe the results of the branching ratio measurement and compare the experimental results with theoretical prediction models. In Sec. VII, we conclude this study and give prospects.

II. SUPER-KAMIOKANDE DETECTOR

A. Detector and data set

The Super-Kamiokande detector is an imaging water Cherenkov detector. It is located 1000 m underground (2700 m of water equivalent) in the Kamioka mine in Gifu prefecture, Japan. The detector components, operation, and performance are detailed in detector papers [48, 49].

The SK detector consists of about 50,000 tonnes of purified water in a stainless steel cylindrical water tank with photomultiplier tubes (PMTs). The detector is divided into two regions by an inner structure that optically separates these regions with sheets. One region is the inner detector (ID) and the other is the outer detector (OD). The ID serves as the target volume for neutrino inter-

actions and the OD is used to veto external cosmic-ray muons as well as γ -rays from the surrounding rock. The ID holds 32,000 tonnes of water as a physics target and its standard fiducial volume (2 m from the inner detector structure) for solar neutrino analysis is 22,500 tonnes. The OD is optically separated from the ID and is used to veto cosmic-ray muons penetrating the mountain above. The ID is viewed by 11129 20-inch PMTs [50] and the OD is viewed by 1885 8-inch PMTs.

The SK data set is separated into eight distinct periods, from SK-I to SK-VIII. For the prior SK-I to SK-V phases, spanning April 1996 to July 2020, the detector operated with ultra-pure water [48]. Starting in July 2020, SK-VI, in which gadolinium sulfate was dissolved into the detector water tank, has been in operation [51]. Then, additional gadolinium loading was conducted in June 2022 [52] toward SK-VII. Table III summarizes the period of operation, the livetime used for this analysis (up to and including SK-VI), the number of ID PMTs, electronics, and the water status.

TABLE III. The summary of data sets used in this analysis. The livetime is the total duration of data samples used for this analysis after removing calibration and bad condition runs.

SK phase	SK-IV	SK-V	SK-VI
Period	Sep. 2008 – May 2018	Jan. 2019 – Jul. 2020	Aug. 2020 – Jun. 2022
ID PMTs			11129
Livetime [days]	2970.1	379.2	552.2
Electronic		QBEE [53, 54]	
Water	Ultra-pure water		Gd loaded water [51]

B. Tagging the stopping muon

In the measurement of unstable isotopes, the tag of the stopping muon is critical to determine the production rate and the branching ratio of nuclear muon capture on oxygen in the SK detector. In this analysis, we developed a method to form pairs of parent stopping muon and decay products from unstable isotopes. In this section, we briefly explain how to tag stopping muons.

1. Electronics up to and including SK-III

From SK-I to SK-III, Analog Timing Modules (ATMs), based on the TKO (Tristan KEK Online) standards, were used as front-end electronics [55, 56]. It generates four types of hardware triggers, called Super Low Energy (SLE), Low Energy (LE), High Energy (HE), and OD. The first three triggers are generated depending on the pulse height of ID PMT signals while the last one is generated when the pulse height of OD PMT signals

exceeds a certain threshold. Once those triggers are generated, a single event is recorded within a $1.3 \mu\text{s}$ timing window.

The observed event is recorded in a $1.3 \mu\text{s}$ window up to and including SK-III. Hence, the parent muon and the decay electron event are recorded separately. However, some charge in the PMT could leak during charge integration after triggering a cosmic-ray muon, such that the number of hit PMTs and hit times are not always correct for subsequent decay electrons, resulting in an inaccurate reconstruction of their energy and timing. For this reason, we have difficulties in reconstructing the stopping muon positions and in forming the pair of the parent muon and the associated decay electron up to and including SK-III. In order to reduce the systematic uncertainties of the analysis presented in this article, we did not use the observed data from SK-I to SK-III.

2. Electronics from SK-IV onwards

For SK-IV, starting in September 2008, new front-end electronics denoted QBEEs [53] were installed. These are capable of very high-speed signal processing, enabling the integration and recording of charge and time for every PMT signal. Since all PMT signals are digitized and recorded, there is no detector deadtime. Furthermore, a new online data acquisition (DAQ) system was implemented which generates multiple software triggers depending on the number of hit PMTs within 200 ns [54]. All PMT signals within a trigger time window are recorded, where the duration of the time window changes depending on the trigger types. Table IV summarizes the trigger types and the duration of an associated single event.

TABLE IV. Summary of software (SK-IV and later) triggers with their timing window to record a single event. AFT trigger is generated when the SHE trigger is issued without the OD trigger in SK-IV [57]. From SK-V onwards, AFT trigger is generated whenever SHE trigger is issued [58].

Trigger	Duration [μs] SK-IV and later
SLE	$[-0.5, +0.8]$
LE and HE	$[-5, +35]$
SHE	$[-5, +35]$
AFT	$[+35, +535]$

The new DAQ system generates Super High Energy (SHE) and AFT triggers; the latter records all hits from $[+35, +535] \mu\text{s}$ to detect delayed events such as thermal neutron capture on hydrogen [59, 60] and gadolinium [51]. In the SK-IV phase, this AFT trigger is generated after the SHE trigger with an OD veto to search for 2.2 MeV γ -ray from neutron capture by hydrogen after an inverse β decay of anti-electron neutrinos [57]. From SK-V, we changed the configuration of generating the AFT

trigger to record spallation neutrons along with through-going cosmic-ray muons [58]. Figure 1 shows the software trigger thresholds during the SK-IV, SK-V, and SK-VI phases. The thresholds have been changed depending on the detector conditions, such as background rate, water circulation pattern, accumulated data transfer speed, and the recording data size, etc.

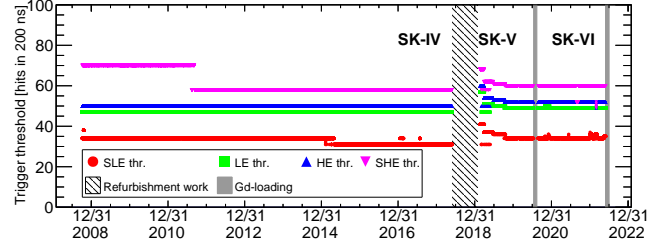


FIG. 1. The software trigger thresholds with the QBEE electronics as a function of time from October 2008 to June 2022. Red circles, light-green squares, blue upper triangles, and pink lower triangles are the SLE, LE, HE, and SHE triggers, respectively [53]. The black left slanting region shows the period of the refurbishment work and the light-gray filled region shows the period of first and second Gd-loading [51, 52].

In this analysis, the selection of the decay electron is critical to find the decays of unstable isotopes due to the nuclear muon capture on oxygen. Except for the SLE trigger, the duration of time windows, as summarized in Table IV, is long enough to capture the vast majority of electrons from muon decay; the corresponding decay electron identification procedure is detailed in Ref. [61]. This long timing window to record a single event is helpful to increase the signal-to-noise ratio to tag the nuclear muon capture events as mentioned in the latter section.

C. Energy calibrations in the MeV region

The energy response of the SK detector is evaluated by several calibration sources. Table V summarizes the calibration sources used in the SK detector, in particular for the energy region below 50 MeV.

TABLE V. Summary of calibration sources used in the SK detector for the MeV energy range.

Calibration source	Purpose
LINAC [62]	Absolute energy scale
DT generator [63]	Position and direction dependence of energy scale
Decay electron [28]	Monitoring water transparency

An absolute energy scale is determined by an electron linear accelerator (LINAC), which was installed at the SK detector to vertically inject mono-energetic electrons from 4.4 MeV to 18.9 MeV with an accuracy on the energy of less than $\pm 0.2\%$ [29, 62]. By comparing the

calibration data against the MC simulation, the absolute energy scale is tuned. However the electron is only injected in the vertical direction and this situation limits the evaluation of the position and direction dependence of the energy scale. To compensate for this situation, another calibration source, a deuterium-tritium neutron (DT) generator, is also used for the evaluation of energy scale [63]. This system generates neutrons via the reaction of $^2\text{H} + ^3\text{H} \rightarrow ^4\text{He} + n$, and the produced neutrons are then captured on oxygen in water. This reaction creates ^{16}N whose final decay products are an electron and a single γ -ray. The DT calibration data has been taken at several positions where the LINAC calibration cannot reach. This allows us to evaluate the systematic uncertainties for the position and direction dependences of the energy scale [29]. Although DT generator can accumulate a large number of β decays, the broad shape of the energy distribution of β decay limits the accuracy for determining the absolute energy scale.

Finally, water transparency is critical for the energy scale because photon propagation depends on its properties, such as the probabilities of absorption, scattering, and reflection [48]. Decay electrons, which are naturally produced by a stopping cosmic-ray muon, are also sampled to evaluate the stability of the detector response. The total amount of observed charge by the PMTs from the decay electrons depends on the quality of water transparency inside the SK detector. In the MC simulation, the parameters for photon propagation are scaled by the observed charge in stopping muon data from decay electrons to reproduce the daily change of real detector response [49].

III. OVERVIEW OF ^{16}N , ^{15}C , ^{12}B , AND ^{13}B DECAYS

In this section, we briefly explain the targets of unstable isotopes due to nuclear muon capture in this analysis. We also summarize the expected production rate of ^{16}N at the SK experimental site, which was computed based on theoretical models by other groups.

A. Production processes and their decay

Soon after the nuclear muon capture process, an excited state of nitrogen, $^{16}\text{N}^*$, is produced in water. Due to the large energy transfer within the multi-body system, energy below 100 MeV is distributed to the compound nucleus. In general, the excited $^{16}\text{N}^*$ emits particles, resulting in the production of various residual nuclei. The evaporation of neutron(s) leads to the production of ^{15}N or ^{14}N [40, 64–67], while in some cases no neutrons are emitted and, for example, ^{16}N may remain after emitting γ -rays. Proton emission results in the production of ^{15}C , and the emission of an α particle results in the production of ^{12}B . Additionally, in rare cases, the emission of

two protons and one neutron produces another isotope, ^{13}B . ^{16}N (with a half-life of 7.13 s) and ^{15}C (with a half-life of 2.45 s) emit electrons and γ -rays, releasing total energies of 10.42 MeV for ^{16}N and 9.77 MeV for ^{15}C , respectively. Figure 2 shows the decay curves of ^{16}N and ^{15}C , and Figure 3 shows the energy spectra of emitted particles. For ^{12}B and ^{13}B , their half-lives and Q -values are 0.0202 s and 13.37 MeV, and 0.0172 s and 13.44 MeV, respectively. Figure 4 shows the decay curves of ^{12}B and ^{13}B . Comparing with the decay curves of ^{16}N and ^{15}C described in Fig. 2, the decay of ^{12}B quickly occurs and fully completes within 0.3 s. Figure 5 shows the energy spectra of emitted particles from ^{12}B and ^{13}B decays.

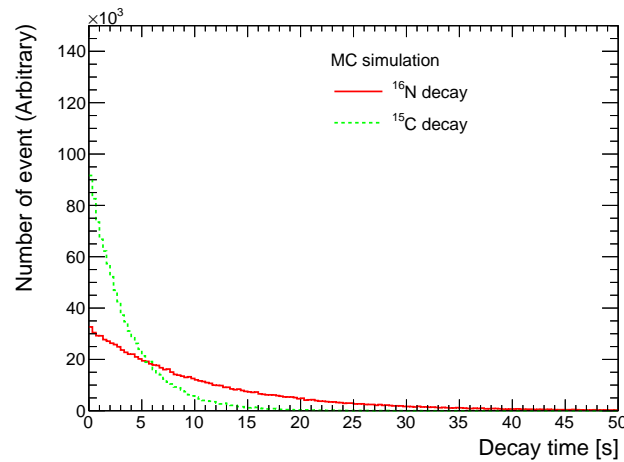


FIG. 2. Examples of the decay curves of ^{16}N and ^{15}C . The red solid line and green dashed lines show the decay curve of ^{16}N and ^{15}C decays, respectively. For comparison purposes, 10^6 decays are simulated for each of the two decays.

B. Predicted production rates

The measurement of production rates of ^{16}N and ^{15}C is important for validating simulation models of muon-induced products at underground experimental sites [68–71]. For example, scintillation experiments such as Borexino, Double Chooz, and KamLAND have measured the production rates of light isotopes through muon captures on nuclei [72–75].

The production rates of unstable isotopes due to muon nuclear capture depend on the depth of the experimental site because the muon nuclear capture process occurs when the cosmic-ray muon stops inside the detector. The change of the number of stopping muons is expected due to the different propagation length of cosmic-ray muons at the underground site. Based on the MUSIC simulation [76], the estimated average energy of cosmic-ray muon is about 270 GeV at the detector site. However, uncertainties in the energy spectrum of primary cosmic-rays, the atmospheric density structure, and the interaction model of QCD cause uncertainties in the intensity

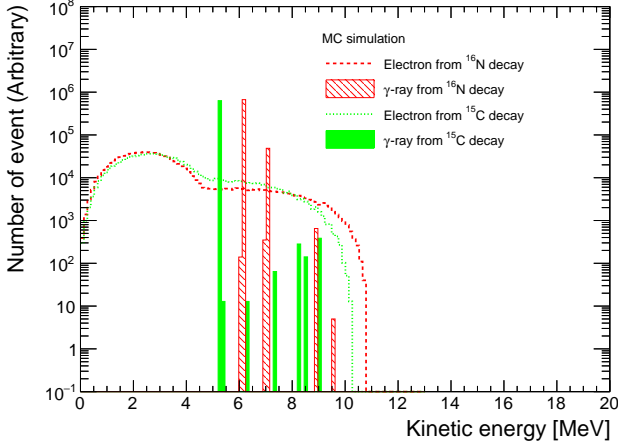


FIG. 3. Kinetic energies of emitted electrons and γ -rays from decays of ^{16}N and ^{15}C . The red dashed and green dotted lines show the energies of electrons from ^{16}N and ^{15}C decays, respectively. The red left-slanting-line histogram and green filled histogram show the energies of γ -rays from ^{16}N and ^{15}C decays, respectively. For comparison purposes, 10^6 decays are simulated for each of the two decays with **Geant4** as detailed in Sec. IV A.

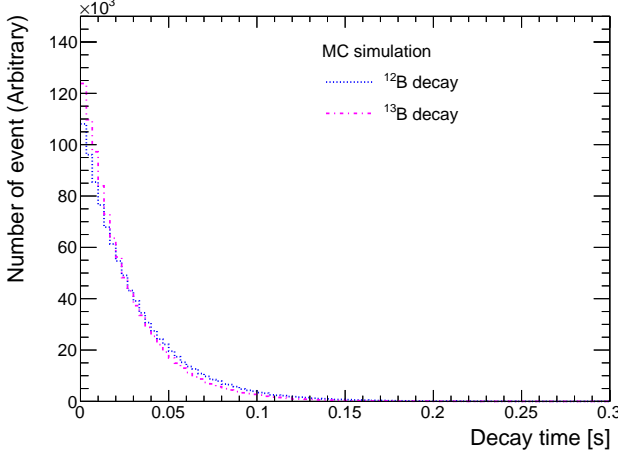


FIG. 4. Examples of the decay curve of ^{12}B and ^{13}B . The blue dotted line and magenta dot-dashed lines show the decay curve of ^{12}B and ^{13}B decays. Comparing with the decay curves of ^{16}N and ^{15}C described in Fig. 2, the decay of ^{12}B quickly occurs and fully completes within 0.3 s. For comparison purposes, 10^6 decays are simulated for each of the two decays.

of cosmic-ray muons and their energy spectrum at the detector site. The production rates of unstable isotopes through muon capture on oxygen nuclei are estimated by simulation-based studies, and then uncertainties are taken into account. Table VI summarizes the expected production rate of ^{16}N produced by the nuclear capture of negative muon on oxygen in the SK detector [68, 69].

Based on the two theoretical predictions, the daily production rate of ^{16}N is small, but the large fiducial volume

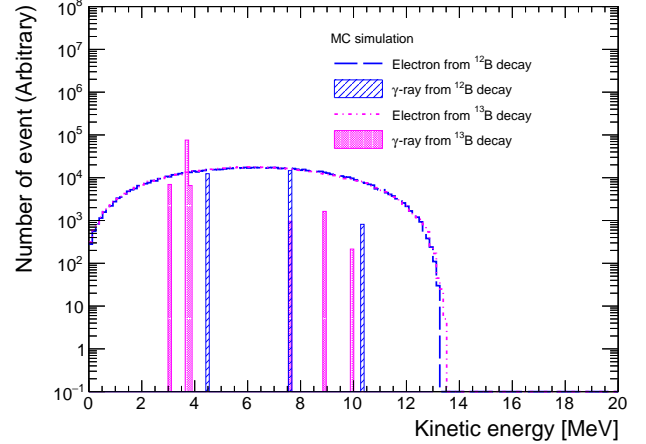


FIG. 5. Kinetic energies of emitted electrons and γ -rays from decays of ^{12}B and ^{13}B . The blue dashed and magenta dot-dashed lines show the energies of electrons from ^{12}B and ^{13}B decays, respectively. The blue right-slanting-line histogram and magenta checkered histogram show the energies of γ -rays from ^{12}B and ^{13}B decays, respectively. For comparison purposes, 10^6 decays are simulated for each of the two decays with **Geant4** as detailed in Sec. IV A.

TABLE VI. Summary of the expected production rate of ^{16}N by the nuclear capture of negative muons in water from the theoretical predictions [68, 69]. No theoretical uncertainty is mentioned in either publication.

Theoretical prediction ^{16}N production rate [event/kton/day]	
C. Galbiati et al. [68]	3.2
S. W. Li et al. [69]	3.0

and the long operation of the SK detector enable us to statistically measure the production rate of ^{16}N . Note that those predictions consider the production rate of ^{16}N only through the nuclear muon capture process on oxygen in water, and other production methods such as spallation production due to through-going muon are not included.

IV. ANALYSIS FOR ^{16}N AND ^{15}C DECAYS

In this section, we present the analysis method and results for measuring the production rates of ^{16}N and ^{15}C in the timing window of $[0.5, 25.0]$ s after the stopping muon. The production rates of ^{12}B and ^{13}B are described in Sec. V.

A. MC simulation

In order to understand the detector response to cosmic-ray muons and the decays of unstable nuclei, a detector

simulation based on the **GEANT3** toolkit [77] was used for this study. This simulation has been tuned by comparing real calibration data with outputs from the MC simulation in SK [49].

The decay kinematics of unstable nuclei are computed using **Geant4** [43, 78, 79] version geant4.10.5p1, with **G4PreCompoundModel** [80] based on Evaluated Nuclear Structure Data Files (ENSDF) version G4ENSDFSTATE2.2 [81]. We simulated the decay times, the momenta of emitting electrons from β decays, and the sequential de-excitation of progeny nuclei, and implemented the detector simulation to evaluate the response of decay products.

As detailed in the next subsections, the stopping-muon and ^{16}N (^{15}C) decay events are separately recorded because of their relatively long half-lives. Therefore, we produced two different simulations: one simulates the stopping muon and the other simulates the ^{16}N and ^{15}C decay events. From the MC simulation for the stopping muon, we evaluate the selection efficiency of the stopping muon inside the fiducial volume. We generated ^{16}N and ^{15}C decay events whose generating vertex positions are taken from the stopping muon MC simulation. By combining two MC simulations, we then evaluate the total selection efficiency for measuring the production rate of ^{16}N and ^{15}C nuclei. Although we can not distinguish ^{16}N decay events from ^{15}C decay events, we can statistically measure the production rates of ^{16}N and ^{15}C by considering the difference in their half-lives and Q -values; this process will be explained in Sec. IV D. For the event generation of the MC simulation, we used the decay time distribution shown in Fig. 2 and the energy spectra shown in Fig. 3.

B. Stopping muon selection

1. Reconstruction of cosmic-ray muon

A decay event of ^{16}N (or ^{15}C , ^{12}B and ^{13}B) is separately recorded from a parent stopping muon since the recorded time of a single event is at most $+535\ \mu\text{s}$ as explained in Sec. II B. We form a possible pair of stopping muon and decay events by considering the combination of timing and spatial information.

The first step of the measurement is selecting the stopping muon events inside the SK detector. The reconstruction of a cosmic-ray muon is performed by a dedicated muon fitter, called the MUBOY algorithm [82, 83]. MUBOY classifies reconstructed muons into four groups depending on the number of muon tracks and the event topology: (I) Single through-going muons, (II) Single stopping muons, (III) Multiple muons, and (IV) Corner-clipping muons. The procedure of reconstructing the stopping muon is detailed in Ref. [61] and their entry position, direction of the muon track, and stopping position are reconstructed. Figure 6 shows the reconstructed stopping muon position in the SK detector.

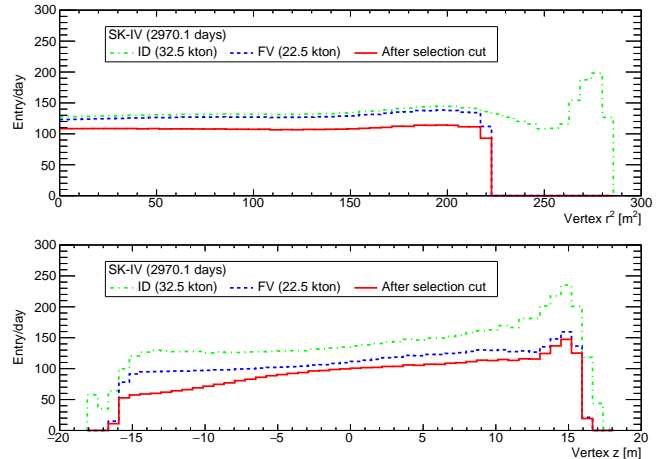


FIG. 6. The distributions of stopping muon positions before and after the muon selection using SK-IV real observed data. The top (bottom) panel shows the distribution of the reconstructed vertex of radius r^2 (height z). The light-green, blue, and red histograms show the number of stopping muons inside the inner detector, inside the fiducial volume, and after the muon selection.

Cosmic-ray muons with a short track inside the detector, as well as corner clipping muons, are sometimes misreconstructed as stopping muons. As detailed in Ref. [61], we optimized the selection criteria to maximize the selection efficiency for stopping muons and to minimize the mis-reconstruction of single-track muons without decays. The selection uses information on the topology of the observed muon such as track length, the total amount of observed charge, the maximum charge of a single PMT, and other reconstruction variables. When the stopping position is close to the detector structure, the MUBOY algorithm can not efficiently tag stopping muons. Based on the muon selection, stopping muons in the fiducial volume are selected with an efficiency of $(65.68 \pm 0.01)\%$ for SK-IV while a single penetrating muon is incorrectly recognized as a stopping muon at a rate less than 0.01%.

Table VII summarizes the selection efficiency for the stopping muon. After the muon selection, the resolution of the reconstructing stopping position inside the fiducial volume is about 50 cm [61].

TABLE VII. Summary of the selection efficiency for stopping muon in the fiducial volume. In this table, the statistical uncertainty of the selection efficiency is listed.

SK phase	Selection efficiency in fiducial volume [%]
SK-IV	65.68 ± 0.01
SK-V	67.35 ± 0.04
SK-VI	67.26 ± 0.03

Figure 7 shows the monthly stopping muon rate before

and after the muon selection. The observed muon rate is basically stable during the SK operation after correcting the selection efficiency.

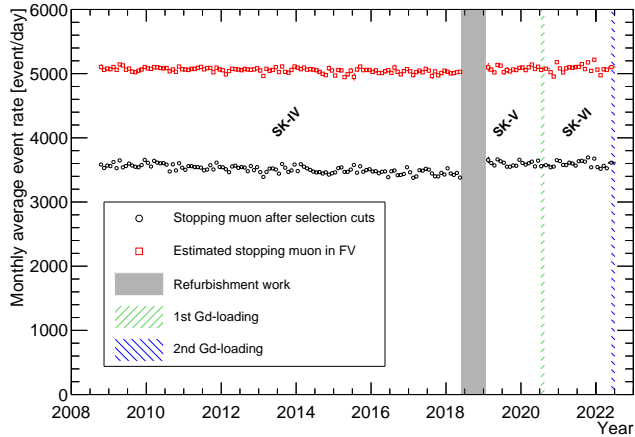


FIG. 7. The monthly average of the number of stopping muons as a function of time. The black open circles show the event rate after the muon selection in units of event/day, and the red open squares show the estimated observed rate after correcting for selection efficiency. We should note that the statistical and systematic uncertainties are smaller than the symbols in this figure. The gray band shows the period of refurbishment work toward SK-Gd [51]. The green (blue) slanting band shows the first (second) Gd loading [51, 52]. In the case of SK-IV, an increase of PMT gain was observed as explained in Ref. [29], which resulted in a change to the cut criteria and a subsequent decrease of muon rate after the muon selection.

Table VIII summarizes the daily observed rates of stopping muons inside the fiducial volume. The observed rates after correcting the selection efficiency among the SK phases are consistent within their uncertainties.

2. Search for decay electron

After installing the new electronics, the duration of the time window to record a single event is long enough to tag a decay electron event after a stopping muon. Hence, we search for a delayed event within the window of $+35\ \mu\text{s}$ after the stopping muon. The majority of non-captured stopping cosmic-ray muons produce their decay electrons and this results in expecting a single delayed event in that search window. Here, we defined the number of delayed events within $+35\ \mu\text{s}$ as N_{trig} . Typically, the decay electron event is recognized as $N_{\text{trig}} = 1$. In contrast, no delayed event in the search window of $+35\ \mu\text{s}$ is expected when a nuclear muon capture occurs. In such a case, $N_{\text{trig}} = 0$ is expected. Figure 8 shows the distribution of N_{trig} associated with observed stopping muons. We should note that $N_{\text{trig}} \geq 2$ sometimes occurs when the accidental noise background event due to radioactive impurities, such as radon, is coincidentally observed within

the timing window of $+35\ \mu\text{s}$. However, the probability of $N_{\text{trig}} \geq 2$ is quite small as demonstrated in Fig. 8.

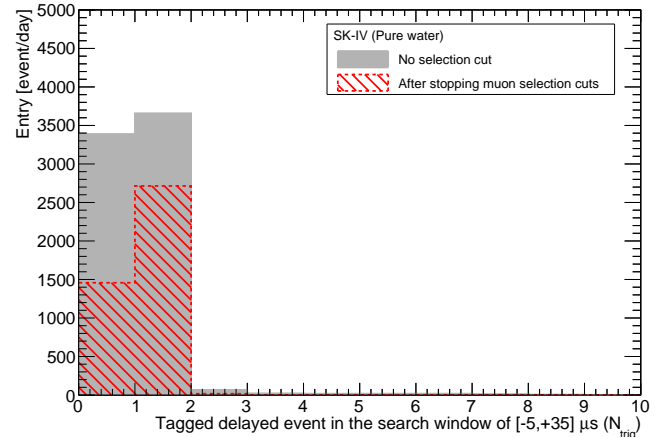


FIG. 8. The distributions of delayed events (N_{trig}) after stopping muons with and without the muon selection using the SK-IV data set. The vertical axis shows the daily number of events before (illustrated in gray filled histogram) and after the muon selection (illustrated in red slanting histogram). The horizontal axis shows the number of delayed events (N_{trig}).

Figure 9 shows the decay time after the stopping muon in the window of $[0.5, 25.0]\ \text{s}$. The sample of $N_{\text{trig}} = 0$ demonstrates that ^{16}N decay candidate events are observed because its half-life is several seconds after stopping muon events are observed, as expected from ^{16}N decays. On the other hand, no ^{16}N decay events are observed when sampling the stopping muon with $N_{\text{trig}} = 1$ and $N_{\text{trig}} \geq 2$. Hence, the distribution in Fig. 9 demonstrates that ^{16}N (as well as ^{15}C) events are successfully tagged by sampling the stopping muons with $N_{\text{trig}} = 0$. Thus, selecting stopping muons with $N_{\text{trig}} = 0$ improves the signal-to-noise ratio of tagging ^{16}N and ^{15}C decay events.

We should note that contamination of N_{trig} sometimes occurs due to an accidental coincidence event just after the stopping muon. We evaluated the systematic uncertainty due to mis-counting the decay signals due to unstable isotopes in Sec. IV E 3.

C. Selection of ^{16}N and ^{15}C decay event

1. Pair construction with stopping muons

Decay events of ^{16}N (and ^{15}C) are recorded separately from stopping muon events due to their long half-lives; such decay events are triggered by SLE, LE, HE, and SHE triggers (listed in Table IV) and reconstructed by a standard reconstruction fitter, called BONSAI [84]. Electrons from ^{16}N decay or those scattered by γ -rays can travel only a few cm in water and the location of the

TABLE VIII. Summary of the daily observed event rate of the stopping muons inside the SK fiducial volume after the muon selection. The uncertainties described in this table are the combination of statistical uncertainties and systematic uncertainty described in Sect. IV E 1 and summarized in Table X.

SK phase	Observed event rate in fiducial volume [event/day]	
	Observed event rate after muon selection	Estimated number of stopping muon corrected by selection efficiency
SK-IV	3512 ± 1 (stat.) ± 30 (syst.)	5347 ± 2 (stat.) ± 46 (syst.)
SK-V	3602 ± 3 (stat.) ± 29 (syst.)	5347 ± 6 (stat.) ± 43 (syst.)
SK-VI	3593 ± 3 (stat.) ± 30 (syst.)	5341 ± 4 (stat.) ± 45 (syst.)

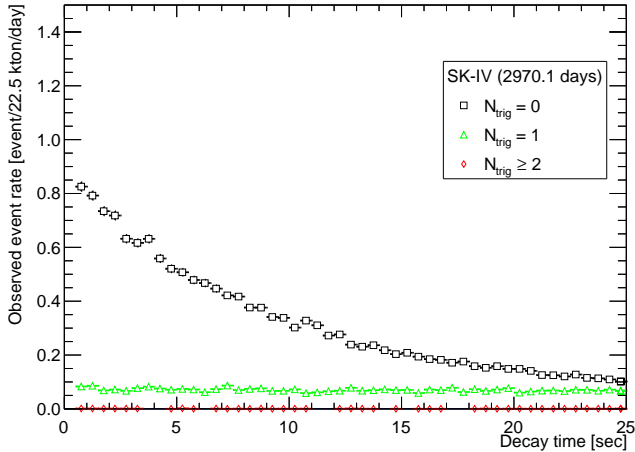


FIG. 9. Decay time distributions in $[0.5, 25.0]$ s with different N_{trig} samples using the SK-IV data set. The black open squares, light-green open triangles, and red open rhombuses show the number of decay candidate events around the stopping muon position with $N_{\text{trig}} = 0$ (without decay electron), $N_{\text{trig}} = 1$ (with decay electron), and $N_{\text{trig}} \geq 2$ (with decay electron and accidental coincidence events), respectively. The sample of $N_{\text{trig}} = 0$ demonstrates that decay candidate events are observed.

Cherenkov emission is recognized as a point. Under this assumption, the vertex position is reconstructed with a maximum likelihood fit of the photon arrival time on the PMTs after subtracting the time of flight from the estimated interaction point [52].

The energy of those events is determined based on the number of hit PMTs with factors to account for delayed hits due to reflection and scattering in water, dark noise on nonhit PMTs, photo-cathode coverage, PMT gain, and water transparency. However, at the stage of the data acquisition, the energy threshold of the accumulated events changes depending on the detector conditions to avoid affecting the data transfer speed as mentioned in Sec. II B. The QBEE electronics, installed at the SK-IV, allow the detector to accumulate more data with high-speed processing. This results in the lowering of the energy threshold at the stage of data acquisition. In this analysis, we set the lower energy threshold of selecting isotope decay events as 4.0 MeV of the reconstructed to-

tal energy of electron.

To efficiently select ^{16}N events, we first collected the stopping cosmic-ray muons and then selected the events that occurred within a certain distance from the stopping position and a relatively long time window after the stopping time. We set the lower limit of the time window as 0.5 s to remove the background events from the decay electrons and the radioactive decays from spallation products, such as ^{12}B and ^{12}N [31, 32]. This selection will also include background events randomly occurring around the stopping muons.

2. Background estimation and subtraction

For selecting the stopping muon, which is captured by oxygen in water, we require $N_{\text{trig}} = 0$ and therefore no delayed signal, such as a decay electron event as well as γ -rays from the excitation ^{14}N and ^{15}N decays within $[-5, +35]$ μs .

Since ^{16}N and ^{15}C decay with relatively long half-lives, the event selection described above can accidentally form an incorrect pair with a stopping muon. Even with the $N_{\text{trig}} = 0$ selection, some decay electrons can be missed due to being too close to the stopping muon in time, and these incorrectly labeled $N_{\text{trig}} = 0$ stopping muons can then form a random coincidence with a delayed signal which is not a muon capture; this would mimic our signal and constitute our background. To estimate the possibility of forming a wrong pair due to the accidental background events, we also collected events within a 24.5 s time window starting 100 s after stopping muons, where this interval is the same length as the time window of the signal selection. Here, we refer to this 100 s delayed window after the stopping muon as the background window. We should note that the selected events in the background window mainly originate from random background events due to radioactive impurities in the water [30] and spallation products induced by through-going muons. Such events will not be correlated with stopping muons with $N_{\text{trig}} = 0$ because of the sufficiently delayed time. Figure 10 shows the decay time distribution after the stopping muon in both the signal window and the background window.

The events in the background window demonstrate that the analysis procedure described above can some-

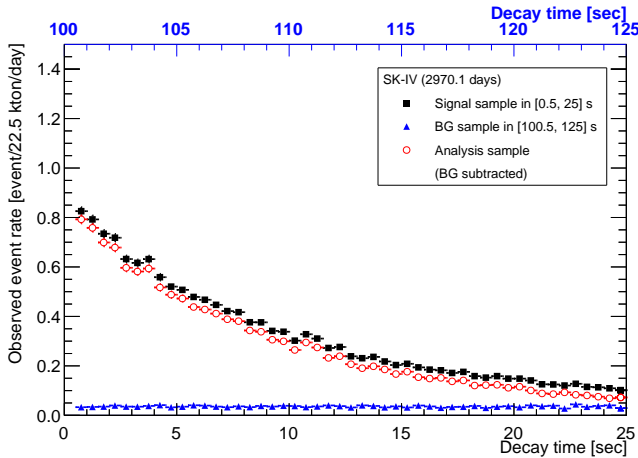


FIG. 10. Decay time distribution of signal sample in $[0.5, 25.0]$ s and background sample in $[100.5, 125.0]$ s after the selection cuts described in Sec. IV C. After subtracting the background distribution from the signal distribution, the analysis sample is produced. The time difference from the stopping muon in the signal region ($[0.5, 25.0]$ s) drawn in black filled squares and the background region ($[100.5, 125.0]$ s with the upper horizontal axis) drawn in blue filled triangles. The analysis sample is drawn in red open circles.

times form an accidental coincidence event with a selected stopping muon. However, the event rate of the background window is flat and smaller than that in the signal window, as shown in Fig. 10. Based on those distributions, the probability of forming a wrong pair due to an accidental background event is small. Hence, we subtracted the event rate in the background window from those in the signal window to reduce the contamination of non- ^{16}N (and ^{15}C) isotope decays.

Figure 11 shows the reconstructed energy distribution in both the signal window and the background window. After subtracting the background distribution, the peak is clearly visible. Hence, the energy distribution after subtracting the background distribution shown in Fig. 11 demonstrates that the ^{16}N and ^{15}C decay events are efficiently selected from the data samples.

3. Optimization of selection cuts

After the initial event reconstruction by BONSAI, several cuts are applied to select the decay candidate events of ^{16}N and ^{15}C . Backgrounds from radioactivity and poorly reconstructed events are seen close to the ID wall. To reduce these backgrounds, events with reconstructed vertices within 2 m from the ID wall (outside of the analysis fiducial volume) are rejected. We also define a backward-projected distance (the distance from the reconstructed vertex to the wall opposite from the direction of travel [25]) and reject events for which this distance is less than 4 m.

In addition to the vertex and timing window cuts, we

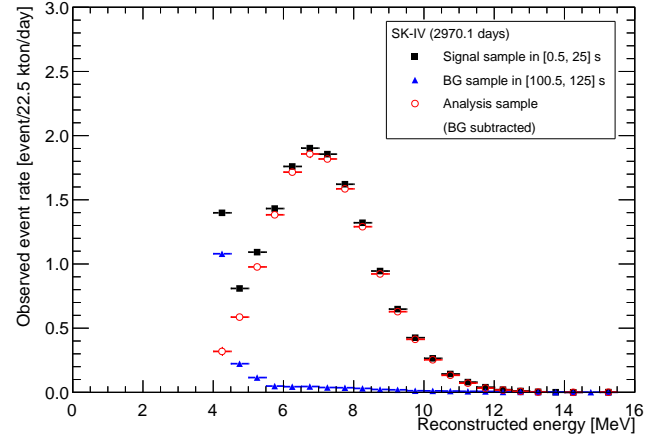


FIG. 11. Reconstructed total energy distribution of signal sample in a $[0.5, 25.0]$ s timing window and background sample in a $[100.5, 125.0]$ s timing window after the selection cuts described in Sec. IV C. After subtracting the background distribution from the signal distribution, the analysis sample is produced. The definition of colors is the same as in Fig. 10.

also apply an event quality cut, for which the quality of event reconstruction is quantified by two variables based on PMT hit timing (g_t) and hit pattern (g_p) [28]. Some radioactive background events, originating mainly from the PMT enclosures, PMT glass, and detector wall structure, are mis-reconstructed inside the fiducial volume even though the true vertex lies outside the fiducial volume. To reject such backgrounds we select events whose $g_t^2 - g_p^2$ is larger than 0.26. Table IX summarizes the selection efficiencies of selection cuts in the SK-IV phase.

In addition to the standard event selection cuts described above, we also optimize the efficiency of forming the pair of the stopping muon and the decay candidate events. To maximize the signal-to-noise ratio to select both ^{16}N and ^{15}C events associated with the nuclear muon capture on oxygen in water, we calculated the significance of the event selection,

$$\text{Significance} = \frac{N_{\text{Signal}}}{\sqrt{N_{\text{Signal}} + N_{\text{BG}}}} \quad (1)$$

where N_{Signal} (N_{BG}) is the number of selected events in the signal timing window (background timing window). This selection considers the different durations of the timing window and the distance between the muon stopping position and the vertex position of decay candidate events. In the case of the signal timing window, both the decay of unstable isotopes and the accidental background events are selected. To remove the background events and improve the purity of the isotope in the analysis sample, we have subtracted the number of background events selected in the background timing window. Figure 12 shows the example of significance curves of the distance cut to select ^{16}N and ^{15}C events near the stop-

TABLE IX. Summary of selection efficiencies for ^{16}N , ^{15}C , ^{12}B , and ^{13}B decay events using the SK-IV MC simulation with a timing window of $[0.5, 25.0]$ s. Here, efficiency of 100% is the generated MC decay events inside the analysis fiducial volume. Note that both ^{12}B and ^{13}B decay events are completely rejected by the timing cut (> 0.5 s) due to their short half-lives. Systematic uncertainties of other phases are summarized in Appendix A.

Selection cut	Selection efficiency [%]			
	^{16}N	^{15}C	^{12}B	^{13}B
1st reduction cut	89.70 ± 0.02	84.12 ± 0.02	83.88 ± 0.02	84.52 ± 0.02
Fiducial volume cut	94.74 ± 0.02	94.16 ± 0.02	93.83 ± 0.02	94.01 ± 0.02
Fit quality cut	86.62 ± 0.02	81.34 ± 0.01	83.52 ± 0.02	84.02 ± 0.01
Effective wall cut	92.81 ± 0.02	92.10 ± 0.02	91.38 ± 0.02	91.57 ± 0.02
Energy cut	90.11 ± 0.02	84.95 ± 0.02	83.46 ± 0.02	84.24 ± 0.02
Timing cut	86.48 ± 0.02	86.59 ± 0.02	0	0
Distance cut	63.58 ± 0.01	61.36 ± 0.01	60.29 ± 0.01	60.90 ± 0.01
Total efficiency	52.34 ± 0.01	46.56 ± 0.01	0	0

ping muon position. Based on this evaluation, we set the distance cut to 160 cm.

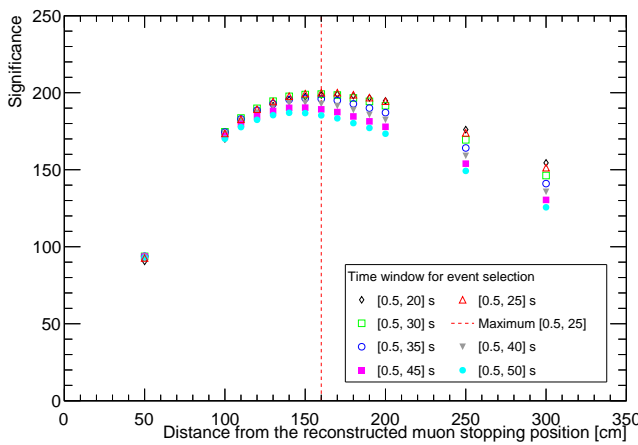


FIG. 12. Significance curves for the event selection of ^{16}N (and ^{15}C) as a function of the distance between the stopping muon and the candidate event positions with different time windows. The plots with different colors and symbols show the significance values with different timing windows using the SK-IV data. The vertical red dashed line shows the maximum significance at 160 cm with $[0.5, 25.0]$ s of the timing window.

D. χ^2 method

To determine the production rates of ^{16}N and ^{15}C via a nuclear muon capture on oxygen in water, the decay times between the stopping muon and the selected event and the energy spectra of the selected events after subtracting the accidental backgrounds are simultaneously fit to the distributions derived from the MC simulation. The definition of total chi-square (χ^2_{Total}) is

$$\chi^2_{\text{Total}} (R_{^{16}\text{N}}, R_{^{15}\text{C}}) = \chi^2_{\text{Time}} + \chi^2_{\text{Energy}} \quad (2)$$

where χ^2 is chi-square for each distribution, $R_{^{16}\text{N}}$ and $R_{^{15}\text{C}}$ are the given production rates for ^{16}N and ^{15}C in unit of event/kton/day, respectively. The χ^2 for each distribution are defined as,

$$\left\{ \begin{array}{l} \chi^2_{\text{Time}} = \sum_i^{n_{\text{Time}}} \frac{(N_i^{\text{Data}} - N_i^{\text{MC}})^2}{(\sigma_i^{\text{Data}})^2 + (\sigma_i^{\text{MC}})^2 + (\sigma_i^{\text{Syst.}})^2} \\ \chi^2_{\text{Energy}} = \sum_i^{n_{\text{Energy}}} \frac{(N_i^{\text{Data}} - N_i^{\text{MC}})^2}{(\sigma_i^{\text{Data}})^2 + (\sigma_i^{\text{MC}})^2} + \left(\frac{1-p}{\sigma^{\text{E-scale}}} \right)^2 \end{array} \right. \quad (3)$$

where N_i^{Data} (N_i^{MC}) is the number of selected events in i -th bin of the observed data (MC) distribution, n is the number of bins, σ_i^{Data} (σ_i^{MC}) is the statistical uncertainty on each bin of the observed data (MC), and $\sigma_i^{\text{Syst.}}$ is the systematic uncertainty on each bin which will be described in Sec. IV E, respectively. Since the energy scale of the detector response affects the value of χ^2_{Energy} , the pull term is introduced only for χ^2_{Energy} , where $\sigma^{\text{E-scale}}$ is the systematic uncertainty of the energy scale determined from LINAC calibration [62]. The details are described in the next section.

E. Systematic uncertainties

In this section, we provide an overview of the systematic uncertainties for the measurement of production rates of ^{16}N and ^{15}C . The systematic uncertainties listed in this section are also used in the analysis for the ^{12}B and ^{13}B measurements.

1. Reconstruction and selection for the stopping muon events

The systematic uncertainties on the number of selected stopping muons are estimated based on MC simulation. The accuracy of the reconstructed stopping muon direction as well as the track length is critical to select the stopping muon event. For direction and track length systematic uncertainties, we estimated the change in number of events which pass our selection based on truth and reconstruction differences in MC simulation and estimated the systematic uncertainty based on this. In addition to the track reconstruction, the observed charge is also critical to selecting the stopping muon. The energy scale of the stopping muon is estimated by its track length in the water tank and the variations are typically at the $\pm 2\%$ level among SK phases [85]. By scaling the observed charge of PMTs in the MC simulation, we estimated the number of events after the muon selection. Table X summarizes the systematic uncertainties to select the stopping muon events. The systematic uncertainties originating from the stopping muon selection are consistent among the three SK phases.

2. Reconstruction and selection cuts for the isotope decay events

In general, the systematic uncertainties of the number of selected events are estimated using calibration data and simulation. To calculate uncertainty on the efficiency of the reduction steps and the accuracy of event reconstruction, calibration data and the MC simulated events are compared by using LINAC [62] and DT calibration devices [63], and a Ni calibration source [49] as used in the solar neutrino analysis [29]. Table XI summarizes the systematic uncertainties on selection cuts determined by comparing calibration data with MC simulation and by shifting the cut parameter values.

3. Mis-counting of N_{trig}

As demonstrated in Fig. 9, the event selection with $N_{\text{trig}} = 0$ clearly improves the signal-to-noise ratio of finding the unstable isotope decays after the stopping muon events. However, the mis-counting of N_{trig} sometimes occurs due to an accidental coincidence event or PMT after-pulse contamination just after stopping muon. To evaluate the mis-counting of N_{trig} , we performed the same analysis procedure on the sample with $N_{\text{trig}} \geq 1$ and then evaluated the number of extra events in the signal sample after subtracting the number of events in the background sample. Table XII summarizes the number of selected events after subtracting the background sample with different N_{trig} .

Even though we selected events with $N_{\text{trig}} \geq 1$, a small excess of the selected events exists in the analysis sample

after subtracting the background sample. To compensate for those events, we assigned the systematic uncertainty on the number of selected events in the analysis sample. We should note that the different relative fractions among the three phases originate from the statistical uncertainties of the selected events after subtracting the background sample from the signal sample. We finally assign the systematic uncertainties on the number of selected events with $N_{\text{trig}} = 0$ as $\pm 1.3\%$, $\pm 5.0\%$, and $\pm 4.0\%$ for the SK-IV, SK-V, and SK-VI samples, respectively.

4. Absolute energy scale

The energy reconstruction (energy scale) is critical in this study to analyze the shape of the energy distribution. The energy reconstruction is tuned by comparing calibration data against MC simulation with LINAC [62] and deuterium-tritium neutron (DT) generator [63] sources. The former determines the absolute energy scale by injecting mono-energetic electron beams and the latter evaluates the directional dependence of the energy scale as well as the stability of the energy scale in time with high statistics radioactive β decays. The energy calibration is explained in detail in Appendix E.

Table XIII summarizes the systematic uncertainties on the energy scale determined by two calibration sources, for each of the SK phases analysed [29]. The relatively large errors for SK-V and SK-VI are a result of the limited number of LINAC calibrations compared to SK-IV, due to their short running times.

5. Charge ratio of cosmic-ray muons

Since a negatively charged muon undergoes nuclear capture by oxygen in water, the fraction of negative muons in the cosmic-ray muon sample affects the measurement of the branching ratio. The charge ratio (R_μ) of cosmic-ray muons is defined as $R_\mu = N_{\mu^+}/N_{\mu^-}$, where N_{μ^+} (N_{μ^-}) is the number of positively (negatively) charged cosmic-ray muons.

The SK detector cannot determine the charge of cosmic-ray muons. However, the SK detector can statistically measure the charge ratio of stopping cosmic-ray muons by evaluating the decay time of paired muons and decay electrons because of the different decay times of positive and negative muons. Table XIV summarizes the charge ratio of cosmic-ray muons measured by the SK detector after installing the new front-end electronics [61].

We used the uncertainties of the charge ratio measurement as the systematic uncertainty of the production rates measurement.

TABLE X. Summary of systematic uncertainties on the number of stopping muon events in SK-IV, SK-V, and SK-VI. The detail of the selection cut is described in Sect. IV B 1 [61].

Selection cut	Systematic uncertainty [%]		
	SK-IV	SK-V	SK-VI
Track length cut	± 0.4	± 0.4	± 0.4
Stopping muon direction cut	± 0.5	± 0.5	± 0.5
Total charge cut	$+0.4/-0.6$	$+0.4/-0.5$	$+0.4/-0.5$
Maximum charge cut	± 0.5	± 0.4	± 0.4
Total systematic uncertainty	$+0.9/-1.0$	$+0.8/-0.9$	$+0.8/-0.9$

TABLE XI. Summary of systematic uncertainties on the number of events for ^{16}N and ^{15}C decay events with the timing window of $[0.5, 25.0]$ s using the SK-IV MC simulation. Systematic uncertainties of other phases are summarized in Appendix A.

Selection cut	Systematic uncertainty [%]	
	^{16}N	^{15}C
1st reduction cut	< 0.1	< 0.1
Fiducial volume cut	± 0.2	± 0.2
Fit quality cut	± 0.4	± 0.2
Effective wall cut	± 0.1	± 0.1
Energy cut	± 0.2	± 0.2
Timing cut	< 0.1	< 0.1
Distance cut	± 0.1	± 0.1
Total	± 0.5	± 0.4

6. Natural abundance of oxygen

Three stable isotopes of oxygen (^{16}O , ^{17}O , and ^{18}O) exist, and their natural abundance should be considered when measuring the production rate of isotopes (as well as the branching ratio). The ratio of formation of muonic atom due to Coulomb force on each element can be expressed by the number of nuclei and the relative probabilities $P(Z)$, where Z is the atomic number, and the parameter $P(Z)$ is experimentally measured [86]. Since they have the same number of protons, $P(Z)$ is the same among the three isotopes. Hence, the systematic uncertainty of the number of nuclear muon captures on oxygen is evaluated based on their natural abundance. According to the NuDat database [87], the dominant component is ^{16}O , whose natural abundance is 99.76% while the small contributions are ^{17}O and ^{18}O , whose natural abundances are 0.04% and 0.20%, respectively.

As listed in Table VIII, the event rate of stopping muons is 5347 ± 2 event/day in the fiducial volume after correcting for the selection efficiency of stopping muons in SK-IV. Then, the number of the nuclear muon captures on oxygen is estimated as 424.1 ± 6.0 event/day after additionally considering the charge ratio of stopping muons [61] and the probability of nuclear muon capture by oxygen, which is expressed as $P_{\text{cap}} = (18.44 \pm 0.01)\%$ [88]. Considering the natural abundances, we estimated the number of nuclear muon captures as

423.0 event/day on ^{16}O , 0.2 event/day on ^{17}O , and 0.9 event/day on ^{18}O , respectively. Table XV summarizes the estimated number of nuclear muon captures on ^{16}O , ^{17}O , and ^{18}O .

Based on the calculation above, the sum of nuclear muon captures by ^{17}O and ^{18}O is smaller than the total uncertainty of nuclear muon capture on ^{16}O . Therefore, we ignored their contributions in this study.

7. Nuclear capture after gadolinium loading

As briefly mentioned in Sec. II A, the SK-VI phase started after the first gadolinium loading in July 2020. During this loading work, 13 tons of $\text{Gd}_2(\text{SO}_4)_3 \cdot 8\text{H}_2\text{O}$ was dissolved, resulting in 0.021% of $\text{Gd}_2(\text{SO}_4)_3$ concentration in the SK tank [51]. These additional elements may produce additional muonic atoms instead of oxygen in water.

As detailed in Ref. [61], the fraction of such additional muonic atoms is small, and their production rate is smaller than that of nuclear muon capture by oxygen in water. We ignored their contribution in this analysis.

F. Measurement of production rates of ^{16}N and ^{15}C

To determine the production rates of naturally produced ^{16}N and ^{15}C through the nuclear muon capture on oxygen in water, we calculated the χ^2 defined in Eq. (2) and then extracted the difference between each value and the minimum value of χ^2 , which is expressed as $\Delta\chi^2(R_{^{16}\text{N}}, R_{^{15}\text{C}}) = \chi^2(R_{^{16}\text{N}}, R_{^{15}\text{C}}) - \chi^2_{\text{Min}}$, where χ^2_{Min} is the minimum value of χ^2 . Figure 13 shows the result of $\Delta\chi^2$ calculation using SK-IV, SK-V, and SK-VI data sets. Based on the χ^2 method, we determined the production rates of ^{16}N and ^{15}C . Because non-zero ^{15}C contribution does not explain the decay time and energy distributions, the observed data demonstrate the contribution from ^{15}C decay events. The measured production rates of ^{16}N and ^{15}C are consistent within their estimated uncertainties.

Table XVI summarizes the measured production rates of ^{16}N and ^{15}C among the SK phases. The combined values are $R_{^{16}\text{N}} = 1.71 \pm 0.01$ (stat. + syst.) event/kton/day

TABLE XII. Summary of the number of selected events with the different N_{trig} . In this table, the number of events after subtracting the background sample distribution is listed.

SK phase	Timing window					
	[0.5, 25.0] s			[0.001, 0.5] s		
	$N_{\text{trig}} = 0$	$N_{\text{trig}} \geq 1$	Assigned systematics	$N_{\text{trig}} = 0$	$N_{\text{trig}} \geq 1$	Assigned systematics
SK-IV	41624	533	$\pm 1.3\%$	7504	113	$\pm 1.5\%$
SK-V	4755	237	$\pm 5.0\%$	932	38	$\pm 4.1\%$
SK-VI	6664	269	$\pm 4.0\%$	1267	60	$\pm 4.7\%$

TABLE XIII. Summary of systematic uncertainties on the energy scale, determined by the LINAC and DT calibrations [29, 62, 63].

SK phase	Systematic uncertainty [%]
SK-IV [29]	± 0.48
SK-V [61]	± 0.87
SK-VI [61]	± 1.32

TABLE XIV. The summary of the charge ratio ($R_{\mu} = N_{+}/N_{\mu-}$) measured by the SK detector [61]. As explained in Sec. II B 1, such a measurement could not be performed up to and including SK-III due to electronics performance.

Phase	Charge ratio (R_{μ})
SK-IV	1.32 ± 0.03
SK-V	1.26 ± 0.07
SK-VI	1.33 ± 0.06
Combined	1.32 ± 0.02

TABLE XV. Summary of the estimated number of nuclear muon capture process on ^{16}O , ^{17}O , and ^{18}O in the analysis fiducial volume (22.5 kton) in a single day. Based on this calculation, the contributions of ^{17}O and ^{18}O are negligible due to their low natural abundance.

SK phase	Nuclear muon capture [event/day]	Estimated number		
		^{16}O	^{17}O	^{18}O
SK-IV	424.1 ± 6.0	423.1	0.2	0.9
SK-V	435.3 ± 13.7	434.3	0.2	0.9
SK-VI	421.8 ± 11.1	420.8	0.2	0.9

and $R_{^{15}\text{C}} = 0.11 \pm 0.01$ (stat. + syst.) event/kton/day, respectively.

Figure 14 shows examples of decay time and energy distributions using the SK-IV data together with their best-fit distributions. The distributions using other SK phases are shown in the Appendix D.

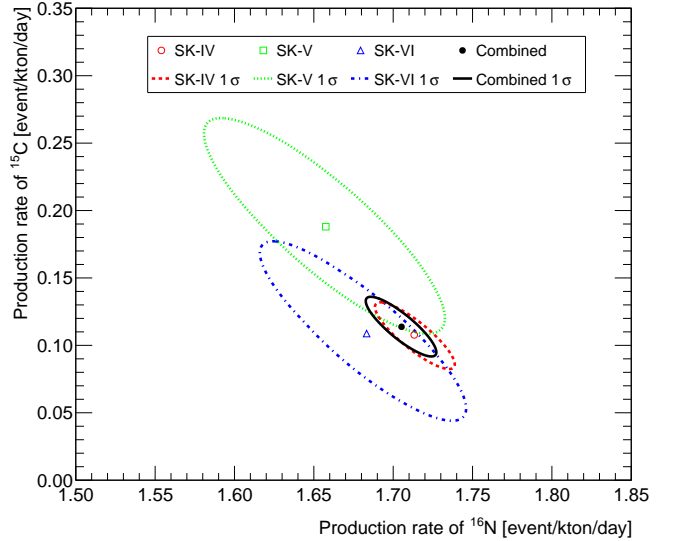


FIG. 13. The 1σ allowed regions of the production rates of ^{16}N and ^{15}C using SK-IV, SK-V, and SK-VI data sets. The red open square (dashed line), green open square (dotted line), and blue open upward-triangle (dashed-dotted line) show the best-fit values (their 1σ allowed regions determined by $\Delta\chi^2 (R_{^{16}\text{N}}, R_{^{15}\text{C}}) = 2.30$) of SK-IV, SK-V, and SK-VI, respectively. The black filled circle (solid line) shows the combined value (1σ allowed region).

G. Comparison with theoretical predictions

In order to test the theoretical predictions as introduced in Sec III, we compared the measured production rates with them. Figure 15 shows the comparison of the production rate of ^{16}N measured by the SK detector with theoretical predictions. The combined production rate of ^{16}N is 1.71 ± 0.01 (stat. + syst.) event/kton/day, where we merged the measurement results from SK-IV, SK-V, and SK-VI. Comparing the measured production rates with the theoretical predictions [68, 69], the estimated production rate is roughly a factor of two larger than that measured in this study.

To properly compare theoretical and experimental production rates, differences in stopping muon rates must be understood. Theoretical predictions consider only vertically down-going muons in their calculation. For the

TABLE XVI. Summary of the production rates of ^{16}N and ^{15}C in water measured by the SK detector. The uncertainties shown in this table include both statistical and systematic uncertainties.

SK phase	Production rate [event/kton/day]	^{16}N	^{15}C
SK-IV	1.71 ± 0.02	0.11 ± 0.02	
SK-V	1.66 ± 0.05	0.19 ± 0.05	
SK-VI	1.68 ± 0.04	0.11 ± 0.04	
Combined	1.71 ± 0.01	0.11 ± 0.01	

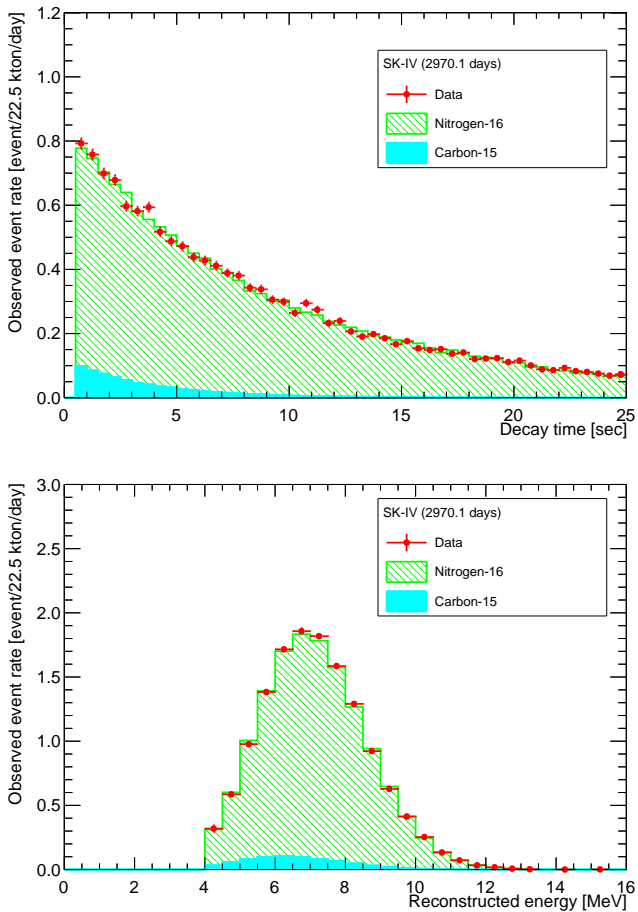


FIG. 14. Distributions of the time difference (top) in the timing window of $[0.5, 25.0]$ s and the reconstructed total energy (bottom) together with the best fit of the components from ^{16}N and ^{15}C using the SK-IV data. Red-filled circles show the observed data after the selection cuts. The light-green right slanting histogram and the light-blue filled histogram show the best fit of ^{16}N , and ^{15}C components, respectively. The distributions of other phases are shown in Appendix D.

theoretical predictions, the average track length is about 32.2 m, and muons with energies below 6.4 GeV at the experimental site are recognized as stopping muons. This corresponds to 5% of cosmic-ray muons reaching the SK detector. In a realistic situation, muons with non-vertical angles can also be detected, and the measured average track length is about 24.3 m [58]. Based on this value, muons with energies below approximately 4.8 GeV will stop inside the detector, which corresponds to 3% of cosmic-ray muons. Taking into account the differences in the stopping muon rates, the theoretical predictions for the production rates of ^{16}N are corrected to about 1.9 event/kton/day [68] and 1.8 event/kton/day [69], respectively. This consideration of stopping muon rate significantly reduces the discrepancy between the predictions and measurements, as shown in Fig. 15. However, there still exists a difference between the measurement and predictions. This remaining discrepancy suggests that the simulation of the production of radioactive isotopes be updated by including this measurement result.

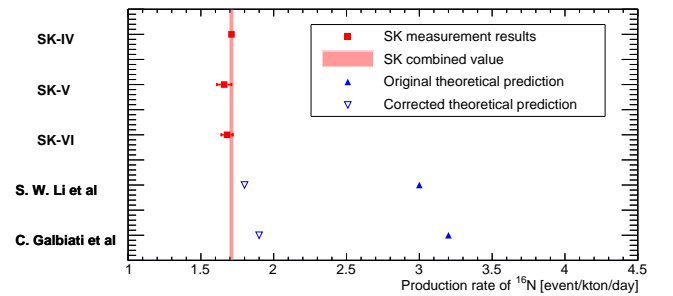


FIG. 15. Comparison of the measurement of the production rate of ^{16}N through nuclear muon capture in water with the predictions from two theoretical models [68, 69]. The red square points show the measured production rate of ^{16}N , the red band shows the combined value of the SK measurement (range of 1σ), the blue filled upward-triangle points show the original theoretical predictions, and the blue open downward-triangle points show the corrected theoretical predictions by considering the topology of stopping muon track at the SK experimental site.

V. ANALYSIS FOR ^{12}B AND ^{13}B DECAYS

In this section, we present the analysis method and the result of measuring the production rates of ^{12}B and ^{13}B in the timing window of $[0.001, 0.5]$ s after the stopping muon. We basically follow the procedure of the decay event selection for ^{16}N and ^{15}C measurements as described in Sect. IV C.

A. Analysis for ^{12}B and ^{13}B measurement

As demonstrated in Fig. 4, both the ^{12}B and ^{13}B decay events are expected to be observed within 0.5 s after stopping muons due to their short half-lives. To evaluate the detector response of ^{12}B and ^{13}B decay events using the MC simulation, we generated their decays based on distributions shown in Fig. 4 and Fig. 5. The selection of both decays is performed by sampling the events within a relatively short time window after stopping muons. For the range of the timing window, we set the upper limit of 0.5 s so that the time interval of the ^{16}N and ^{15}C measurement does not overlap with it. We also set the lower limit of 0.001 s because of the following reasons: After installing the new electronics in SK-IV onwards, the DAQ system generates the additional trigger (AFT trigger), whose range of recording delayed events is at most 535 μs . We use the time window of $[0.001, 0.5]$ s for measuring the production rates of ^{12}B and ^{13}B isotopes. Because the measured four isotopes have similar Q -values, the vertex resolutions of selected decay events do not change even in the different timing windows. Hence, the distance cut (160 cm) is the same as that for ^{16}N and ^{15}C measurements. Other selection criteria are also optimized by following the procedure described in Sect. IV C 3.

Table XVII summarizes the selection efficiencies for the timing window of $[0.001, 0.5]$ s. Although the duration of the timing window is short, background events from ^{16}N and ^{15}C exist in the window.

We also estimated the systematic uncertainties for ^{12}B and ^{13}B measurements. Table XVIII summarizes the systematic uncertainty of the selection cuts. Other systematic uncertainties are the same as those described in Sec. IV E.

B. χ^2 method for ^{12}B and ^{13}B measurement

To determine the production rates of ^{12}B and ^{13}B isotopes, the χ^2 calculation described in Eq. (2) is modified by introducing the contribution of ^{12}B and ^{13}B decays as following;

$$\begin{aligned} \chi^2_{\text{Total}} (R_{^{16}\text{N}}^{\text{Best}}, R_{^{15}\text{C}}^{\text{Best}}, R_{^{12}\text{B}}, R_{^{13}\text{B}}) \\ = \chi^2_{\text{Time}} + \chi^2_{\text{Energy}} \\ + \left(\frac{(1 - \alpha) N_{^{16}\text{N}}^{\text{Best}}}{\sigma_{^{16}\text{N}}^{\text{Best}}} \right)^2 + \left(\frac{(1 - \beta) N_{^{15}\text{C}}^{\text{Best}}}{\sigma_{^{15}\text{C}}^{\text{Best}}} \right)^2 \end{aligned} \quad (4)$$

where $R_{^{12}\text{B}}$ ($R_{^{13}\text{B}}$) is the production rate of ^{12}B (^{13}B) to be measured by this method, $R_{^{16}\text{N}}^{\text{Best}}$ ($R_{^{15}\text{C}}^{\text{Best}}$) is the measured production rate in ^{16}N (^{15}C) by the analysis described in Sec. IV above, χ^2_{Time} and χ^2_{Energy} are the same ones defined in Eq. (3), $\sigma_{^{16}\text{N}}^{\text{Best}}$ ($\sigma_{^{15}\text{C}}^{\text{Best}}$) is the total uncertainty of production rate as summarized in Table XVI, $N_{^{16}\text{N}}^{\text{Best}}$ ($N_{^{15}\text{C}}^{\text{Best}}$) is the estimated number of decay events in the analysis sample after the selection cuts for ^{16}N (^{15}C),

and a parameter α (β) is a scaling factor for the fluctuation of the number of $N_{^{16}\text{N}}^{\text{Best}}$ ($N_{^{15}\text{C}}^{\text{Best}}$) decay events in the signal region.

C. Measurement of production rates of ^{12}B and ^{13}B

To determine the production rates of naturally produced ^{12}B and ^{13}B through the nuclear muon capture on oxygen in water, we calculated the χ^2 defined in Eq. (4) and followed procedure outlined in Sec. IV F. Figure 16 shows the result of the $\Delta\chi^2$ calculation using SK-IV, SK-V, and SK-VI data sets.

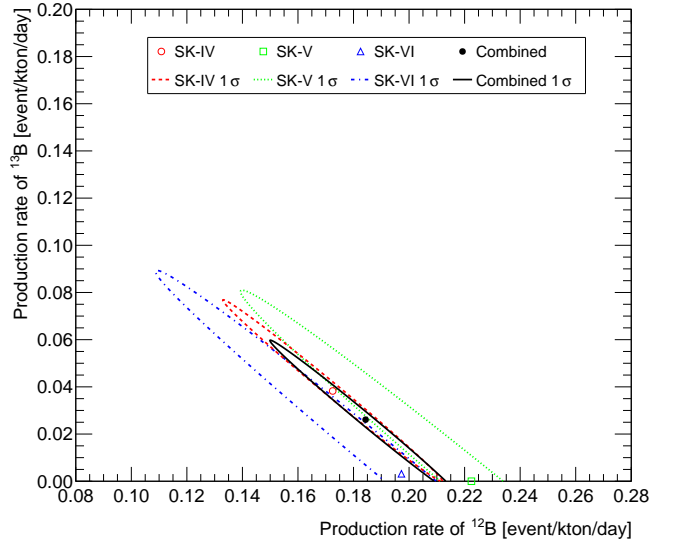


FIG. 16. The allowed regions of the production rates of ^{12}B and ^{13}B using SK-IV, SK-V, and SK-VI data sets calculated by Eq. (4). The red open square (dashed line), green open square (dotted line), and blue open upward-triangle (dashed-dotted line) show the best-fit values (their 1σ allowed regions determined by $\Delta\chi^2$ ($R_{^{12}\text{B}}, R_{^{13}\text{B}}$) = 2.30) of SK-IV, SK-V, and SK-VI, respectively. The black filled circle (solid line) shows the combined value (1σ allowed region).

Table XIX summarizes the measured production rates of ^{12}B and ^{13}B isotopes among the SK phases. The values obtained when combining the SK phases are $R_{^{12}\text{B}} = 0.18 \pm 0.02$ event/kton/day, and $R_{^{13}\text{B}} = 0.03 \pm 0.02$ event/kton/day, where uncertainty is both statistical and systematic.

Figure 17 shows examples of decay time and energy distributions using the SK-IV data together with their best-fit distributions. The distributions using other SK phases are shown in Appendix D. Based on the analysis of the SK-IV data sample, we statistically extracted the excess of ^{13}B events over the distributions of ^{16}N , ^{15}C , and ^{12}B , as shown in Fig. 17. However, SK phases other than SK-IV do not have enough statistics to extract ^{13}B events due to their short operation period and the low

TABLE XVII. Summary of selection efficiencies for ^{16}N , ^{15}C , ^{12}B , and ^{13}B decay events using the SK-IV MC simulation with a timing window of $[0.001, 0.5]$ s. Except for the timing cut, the efficiency of selection cuts is the same as Table IX. Selection efficiencies and their uncertainties of other phases are summarized in Appendix A.

Selection cut	Selection efficiency [%]			
	^{16}N	^{15}C	^{12}B	^{13}B
Timing cut ($[0.001, 0.5]$ s)	4.75 ± 0.01	13.30 ± 0.01	96.66 ± 0.02	96.04 ± 0.02
Selection cuts	Same as Table IX			
Total efficiency	2.88 ± 0.01	7.14 ± 0.01	53.78 ± 0.01	54.19 ± 0.01

TABLE XVIII. Summary of systematic uncertainties on the number of events for ^{12}B and ^{13}B decay events with the timing window of $[0.001, 0.5]$ s using the SK-IV MC simulation. Systematic uncertainties of other phases are summarized in Appendix A.

Selection cut	Systematic uncertainty [%]	
	^{12}B	^{13}B
1st reduction cut	< 0.1	< 0.1
Fiducial volume cut	± 0.1	± 0.1
Fit quality cut	± 0.4	± 0.4
Effective wall cut	± 0.1	± 0.1
Energy cut	± 0.1	± 0.1
Timing cut	< 0.1	< 0.1
Distance cut	± 0.2	± 0.1
Total	± 0.4	± 0.4

TABLE XIX. Summary of the production rates of ^{12}B and ^{13}B measured by the SK detector. The uncertainty shown in this table includes both statistical and systematic uncertainties. For the production rate of ^{13}B , we list both the 1σ and 90% C.L. values when the 1σ uncertainty is lower than the mean value, and only the 90% C.L. value otherwise.

SK phase	Production rate		
	[event/kton/day]		
	^{12}B	^{13}B (1σ)	^{13}B (90% C.L.)
SK-IV	0.17 ± 0.03	0.04 ± 0.03	< 0.09
SK-V	$0.22^{+0.01}_{-0.05}$	—	< 0.12
SK-VI	$0.20^{+0.01}_{-0.06}$	—	< 0.13
Combined	0.18 ± 0.02	0.03 ± 0.02	< 0.07

production rate of ^{13}B .

Due to the low production rate of ^{13}B , the sensitivity of the measurement is still limited, where the excess of ^{13}B at the 1σ level as summarized in Table XIX. Hence, further data accumulation is required to precisely measure the production rate of ^{13}B by improving energy and timing resolutions.

VI. MEASUREMENT OF BRANCHING RATIO

A. Measurement of branching ratios

By considering the charge ratio of stopping muons, the number of nuclear muon captures can be estimated. The branching ratio of unstable isotopes can be determined by dividing the production ratio of isotopes by the total number of stopping negative muons with the correction of selection efficiencies. The branching ratio $Br(i)$ of i -th isotope can be expressed as,

$$Br(i) = \frac{R(i) \times V}{N_{\text{stop}}^{\mu} \left(\frac{1}{1+R_{\mu}} \right) P_{\text{cap}}}, \quad (5)$$

where $R(i)$ is the production rate of i -th isotope, V is the fiducial volume of the analysis sample (22.5 kton), N_{stop}^{μ} is the total number of stopping muon inside the fiducial volume, R_{μ} is the charge ratio of stopping muon listed in Table XIV, and P_{cap} is the fraction of nuclear capture by oxygen [88].

Based on the measured production rates described in Sect. IV, we can calculate the branching ratio from Eq. (5). Table XX summarizes the branching ratio measured by the SK detector. By combining the SK measurements, we obtained $Br(^{16}\text{N}) = (9.0 \pm 0.1 \text{ (stat. + syst.)})\%$, $Br(^{15}\text{C}) = (0.6 \pm 0.1 \text{ (stat. + syst.)})\%$, $Br(^{12}\text{B}) = (0.98 \pm 0.18 \text{ (stat. + syst.)})\%$, and $Br(^{13}\text{B}) = (0.14 \pm 0.12 \text{ (stat. + syst.)})\%$, respectively, where the range of their uncertainty is 1σ .

B. Comparison with theoretical predictions and experimental measurements

In this section, we compare the measurement results described in the former sections with the measurements by other groups and the predictions by simulations.

As mentioned in Sec. I, the branching ratio is not fully understood because only a limited number of unstable isotopes have been measured. Figure 18 shows the branching ratios measured by the SK detector together with past measurements by other groups [40, 42] and three simulations.

TABLE XX. Summary of branching ratio of negative muon capture on oxygen nuclei measured by the SK detector. Owing to the low production rate of ^{13}B , the upper limits of the branching ratio are set for SK-IV, SK-V, and SK-VI.

SK phase	Branching ratio [%]				^{13}B (90% C.L.)
	^{16}N	^{15}C	^{12}B	^{13}B (1σ)	
SK-IV	9.1 ± 0.2	0.6 ± 0.1	0.92 ± 0.14	$0.20^{+0.14}_{-0.13}$	< 0.49
SK-V	8.6 ± 0.4	1.0 ± 0.3	$1.1^{+0.1}_{-0.3}$	—	< 0.6
SK-VI	9.0 ± 0.3	0.6 ± 0.2	$1.1^{+0.1}_{-0.3}$	—	< 0.7
Combined	9.0 ± 0.1	0.6 ± 0.1	0.98 ± 0.18	0.14 ± 0.12	< 0.39

For the ^{16}N isotope, the branching ratio measured by the SK detector is consistent with that measured by Ref. [39, 40, 88, 89] within at most 1.9σ . Considering the total uncertainty, the branching ratio measured by the SK detector is three times more accurate than the previous measurement. This measurement of the branching ratio of ^{16}N is currently the most accurate in the world.

For ^{15}C , ^{12}B , and ^{13}B isotopes, these are the first branching ratio measurements and provide new inputs for updating simulations of the nuclear muon capture process.

Figure 19 shows the deviation of the predicted branching ratio from the SK measurement result. Because of high precision measurements, the SK data can test the predicted values extracted from the MC simulation.

In the case of ^{16}N measurement, the SK measurement data completely exclude the predicted values from three simulations, PHITS, Geant4, and Fluka. The ^{15}C measurement is consistent with Geant4 and Fluka simulations within 1σ while excluding the PHITS prediction by 5.3σ . Due to the current accuracy of the measurement, the branching ratio of ^{13}B is consistent with PHITS and Fluka within 1σ . Finally, the ^{12}B measurement is consistent with the PHITS simulation within 1σ while completely excludes the Geant4 and Fluka predictions.

We suggest that further improvement of simulations for muonic capture processes is required for future studies based on those measurement results.

C. Comparison with the neutron multiplicity measurement in SK-VI

In an independent analysis, we measured the neutron multiplicity in the nuclear muon capture reaction using the SK-VI data set [66]. This measurement utilizes γ -rays emitted from $\text{Gd}(n, \gamma)$ reactions to detect free neutrons. In the stopping muon sample, we counted the number of detected neutrons per event, and the observed distribution is corrected with the neutron detection efficiency and the false-positive rate by a χ^2 method. The corrected distribution is scaled by the expected number of nuclear muon capture events in the sample to obtain branching ratios for each neutron multiplicity. As a result, the probability $P(i)$ of i neutrons emitted in the nuclear muon capture process on oxygen is obtained to be

$P(0) = (24 \pm 3)\%$, $P(1) = (70^{+3}_{-2})\%$, $P(2) = (6.1 \pm 0.5)\%$, and $P(3) = (0.38 \pm 0.09)\%$, respectively.

When the isotopes measured in the main text are produced in the nuclear muon capture, no neutron is expected to be emitted for ^{16}N , ^{15}C , and ^{12}B isotopes, while one neutron is expected for the ^{13}B isotope, as summarized in Table II. The total branching ratio for ^{16}N , ^{15}C , and ^{12}B in this measurement is 10.6% and is around half of $P(0)$ from the neutron measurement. That indicates other branches contribute to $P(0)$ with a large fraction.

The measurement of isotope production, together with the neutron multiplicity measurement, can provide inputs for theoretical studies of nuclear structure on light nuclei.

VII. SUMMARY AND PROSPECTS

The measurement of production rates of isotopes produced by a nuclear muon capture can validate models of background due to muons in underground detectors and provide input for the simulation of nuclear structure. We selected stopping muons in the SK detector and successfully measured the production rates of ^{16}N , ^{15}C , ^{12}B , and ^{13}B as $R_{^{16}\text{N}} = 1.71 \pm 0.01$ (stat. + syst.) event/kton/day, $R_{^{15}\text{C}} = 0.11 \pm 0.01$ (stat. + syst.) event/kton/day, $R_{^{12}\text{B}} = 0.18 \pm 0.02$ (stat. + syst.) event/kton/day, and $R_{^{13}\text{B}} = 0.03 \pm 0.02$ (stat. + syst.), respectively. Those measurements are useful in the SK experiment for modeling the realistic background due to muons overlapped with solar neutrinos, diffuse supernova neutrino background, and reactor neutrinos.

Based on the production rates of the unstable isotopes, we measured the branching ratio as $Br(^{16}\text{N}) = (9.0 \pm 0.1 \text{ (stat. + syst.)})\%$, $Br(^{15}\text{C}) = (0.6 \pm 0.1 \text{ (stat. + syst.)})\%$, $Br(^{12}\text{B}) = (0.98 \pm 0.18 \text{ (stat. + syst.)})\%$, and $Br(^{13}\text{B}) = (0.14 \pm 0.12 \text{ (stat. + syst.)})\%$, respectively. The result for ^{16}N is the most precise measurement at present and consistent with past results measured by other groups within 1.9σ . The results for ^{15}C , ^{12}B , and ^{13}B are the first measurements of branching ratios of those isotopes.

Based on those measurement results, we suggest that further improvement of simulations for muonic capture processes is required for future studies. The measure-

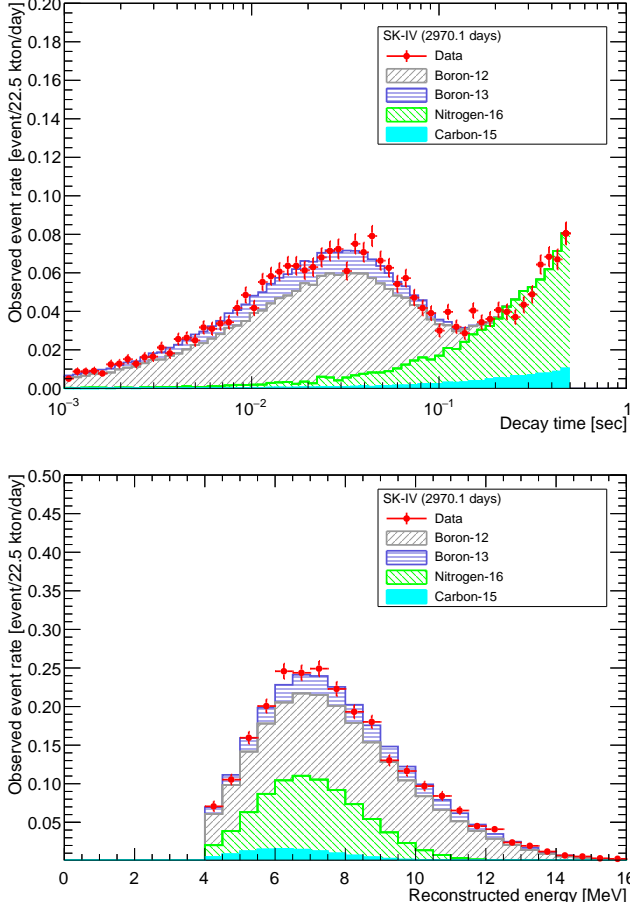


FIG. 17. Distributions of the time difference (top) in the timing window of $[0.001, 0.5]$ s and the reconstructed energy (bottom) together with the best-fit of the components from ^{12}B , ^{13}B , ^{16}N , and ^{15}C using the SK-IV data. Red filled circle shows the observed data after the selection cuts. Light-gray left slanting histogram, light-purple horizontal lines histogram, light-green right slanting histogram, and light-blue filled histogram show the best-fit of ^{12}B , ^{13}B , ^{16}N , and ^{15}C components, respectively. The distributions for other SK phases are shown in Appendix D.

ment results are also helpful to test theoretical models, which calculate muon capture rates with the momentum transfer near the muon mass, and to further study low-energy neutrino-nucleus reactions [90].

We also suggest that the modeling of background due to muons in underground experiments be tuned and updated according to the measured production rates of unstable isotopes resulting from nuclear muon capture. Such updates are helpful to improve the sensitivities for astrophysical neutrinos, such as solar neutrinos, diffuse supernova neutrino background, etc.

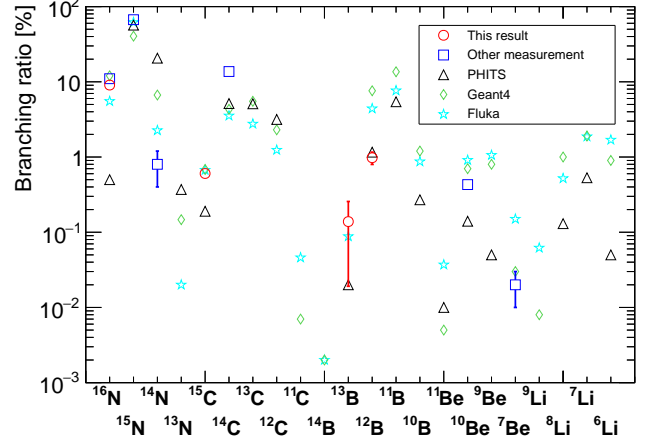


FIG. 18. Comparison of measured branching ratio through nuclear muon capture in water. Red circles show the result measured by the SK detector, blue squares show the other measurement results, and other symbols show simulated values from PHITS, Geant4, and Fluka, as summarized in Table I.

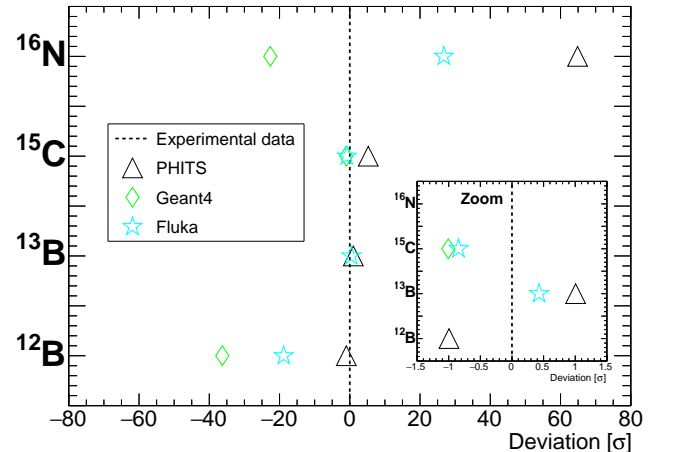


FIG. 19. Deviations between the experimental data and the predicted branching ratios of ^{16}N , ^{15}C , ^{13}B and ^{12}B from three MC simulations, such as PHITS, Geant4, and Fluka. The definition of symbols and color is the same as Fig. 18. The inset panel shows a zoomed-in figure around zero deviation. Note that Geant4 does not produce ^{13}B as listed in Table I. Hence, no point is plotted.

ACKNOWLEDGMENT

We would like to thank M. Niikura from RIKEN Nishina Center for Accelerator-Based Science for suggestions about the decay modes of boron associated with nuclear muon captures on oxygen. We also thank S. Abe from Nuclear Science Research Institute, Japan Atomic Energy Agency for providing their calculation results

of the branching ratio by using PHITS. We also thank J.F. Beacom and O. Nairat from Ohio State University for providing their calculation results of the branching ratio by using Fluka, and their helpful comments and suggestions relating to the production rate of ^{16}N described in Sec. IV G.

We gratefully acknowledge the cooperation of the Kamioka Mining and Smelting Company. The Super-Kamiokande experiment has been built and operated from funding by the Japanese Ministry of Education, Culture, Sports, Science and Technology; the U.S. Department of Energy; and the U.S. National Science Foundation. Some of us have been supported by funds from the National Research Foundation of Korea (NRF-2009-0083526, NRF-2022R1A5A1030700, NRF-2022R1A3B1078756, RS-2025-00514948) funded by the Ministry of Science, Information and Communication Technology (ICT); the Institute for Basic Science (IBS-R016-Y2); and the Ministry of Education (2018R1D1A1B07049158, 2021R1I1A1A01042256, RS-2024-00442775); the Japan Society for the Promotion of Science; the National Natural Science Foundation of China under Grants No. 12375100; the Spanish Ministry of Science, Universities and Innovation (grant PID2021-124050NB-C31); the Natural Sciences and Engineering Research Council (NSERC) of Canada; the Scinet and Digital Research of Alliance Canada; the National Science Centre (UMO-2018/30/E/ST2/00441 and UMO-2022/46/E/ST2/00336) and the Ministry of Science and Higher Education (2023/WK/04), Poland; the Science and Technology Facilities Council (STFC) and Grid for Particle Physics (GridPP), UK; the European Union's Horizon 2020 Research and Innovation Programme H2020-MSCA-RISE-2018 JENNIFER2 grant agreement no. 822070, H2020-MSCA-RISE-2019 SK2HK grant agreement no. 872549; and European Union's Next Generation EU/PRTR grant CA3/RSUE2021-00559; the National Institute for Nuclear Physics (INFN), Italy. This work is partially supported by MEXT KAKENHI Grant Numbers 24K00654 and 24H02243.

Appendix A: Selection efficiencies among the SK phases

In the main text, the cut criteria and the selection efficiencies for isotope decay events are described using the SK-IV data because of that phase's long and stable operation. In this appendix, we summarize the cut criteria and selection efficiencies for each SK phase.

Based on the significance value defined in Eq. (1), we determined the selection criteria for both the distance cut and the time window. Among SK phases, the selection criteria are the same, which are explained in Sec. IV C 3. We also optimized the selection cuts in the same manner. Table XXI shows the selection efficiencies among the three SK phases for the search window of [0.5, 25.0] s. The selection efficiencies in both SK-V and SK-VI are

lower than that in SK-IV because of the worse ID PMT response under single electron yield. In particular, the timing resolution of the PMT was changed in SK-V onwards due to the change of the high-voltage setting of the ID PMTs.

TABLE XXI. Summary of the selection efficiency for the timing window of [0.5, 25.0] s among the SK phases. As explained in Sec. IV, the decay events of ^{12}B and ^{13}B are completely rejected by the timing cut because of their relatively short lifetimes.

SK phase	Selection efficiency [%]	
	^{16}N	^{15}C
SK-IV	52.34 ± 0.01	46.56 ± 0.01
SK-V	45.43 ± 0.05	38.57 ± 0.05
SK-VI	44.76 ± 0.04	37.81 ± 0.04

Table XXII shows the selection efficiencies among the three SK phases for the search window of [0.001, 0.5] s. The differences in efficiency between periods can be explained by the same reason mentioned above.

Appendix B: Systematic uncertainties for the event selection cuts

In Sect. IV E we show the list of systematic uncertainties caused by the selection cuts in SK-IV data set. Here, we list the estimated systematic uncertainties in other SK phases. Table XXIII summarizes the total systematic uncertainties originating from the selection cuts of isotope decay events.

Appendix C: N_{trig} distributions in SK-V and SK-VI data sets

In the main text, we show the distributions using SK-IV data set since the livetime is the longest among the three SK phases. Figure 20 shows the N_{trig} distributions using the SK-V and SK-VI data sets. Comparing the distributions with those in the SK-IV phase, no clear change was observed. In particular, gadolinium loading from SK-VI onwards does not affect the distribution [52].

Appendix D: Distributions of other SK data samples

In this section, the energy and the decay time distributions measured by the SK phases are shown except for the SK-IV phase which was already shown in the main text.

Figure 21 shows the distributions of the decay time and the energy in the time window of [0.5, 25.0] s using the SK-V sample.

TABLE XXII. Summary of the total selection efficiency for the timing window of $[0.001, 0.5]$ s among the three SK phases. The details of selection cuts are summarized in Table IX. As explained in Sec. V, some of ^{16}N and ^{15}C decays enter into this timing window due to their relatively long lifetimes.

SK phase	Selection efficiency [%]			
	^{16}N	^{15}C	^{12}B	^{13}B
SK-IV	2.88 ± 0.01	7.14 ± 0.01	53.78 ± 0.01	54.19 ± 0.01
SK-V	2.47 ± 0.01	5.90 ± 0.02	47.95 ± 0.06	48.23 ± 0.06
SK-VI	2.43 ± 0.01	5.81 ± 0.01	47.39 ± 0.05	47.74 ± 0.05

TABLE XXIII. Summary of total systematic uncertainties originating from the selection cuts of the isotope decay events. The list of the selection cuts is described in Table XI and Table XVIII.

SK phase	Total systematic uncertainties [%]			
	^{16}N	^{15}C	^{12}B	^{13}B
SK-IV	± 0.5	± 0.4	± 0.4	± 0.4
SK-V	± 1.4	± 1.9	± 1.0	± 1.0
SK-VI	± 1.5	± 1.8	± 1.1	± 1.1

Figure 22 shows the distributions of the decay time and the energy in the $[0.001, 0.5]$ s time window using SK-V sample.

Figure 23 shows the distributions of the decay time and the energy in the time window of $[0.5, 25.0]$ s using SK-VI sample.

Figure 24 shows the distributions of the decay time and the energy in the time window of $[0.001, 0.5]$ s using SK-VI sample.

Appendix E: Energy scale evaluation using ^{16}N and ^{15}C sample

Since ^{16}N (and ^{15}C) isotope is naturally produced via a negative muon capture on oxygen nuclei in the water during the usual operation of the SK detector, their decays produce background events when their energies overlap those of solar neutrinos, diffuse supernova neutrinos, and reactor neutrinos. However, selecting such pure samples of isotopes with long lifetimes allows us to monitor the stability of the energy scale in the MeV region of the detector. Furthermore, the position and direction dependence of the energy scale can be evaluated by analyzing these isotopes because the nuclear capture process occurs throughout the detector volume, as shown in Fig. 6, and the decay particles are isotropically emitted [63, 91]. For that purpose, we collected ^{16}N (and ^{15}C) decay events as the natural source sample, and we evaluated the energy scale during the usual operation of the SK detector. Then, we demonstrate the consistency of the energy scale with another calibration source, e.g., the DT generator [63], in this Appendix.

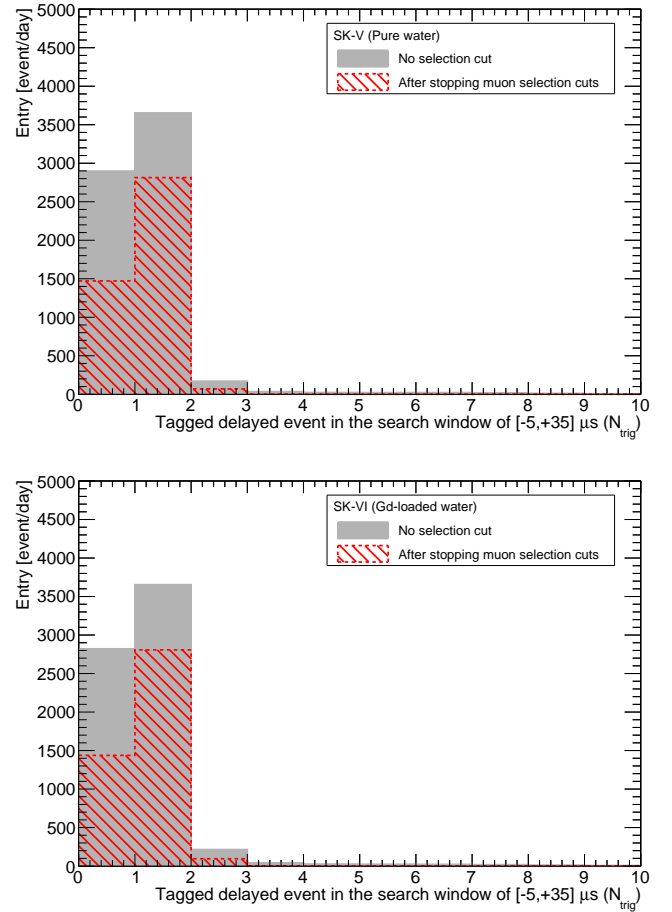


FIG. 20. The distributions of delayed events (N_{trig}) after stopping muons with and without the selection cuts using the SK-V (top) and SK-VI (bottom) data sets. The daily observed rates of stopping muons without the delayed signal ($N_{\text{trig}} = 0$) are consistent within their uncertainty.

1. Monitoring the energy scale

For monitoring purposes, we first selected ^{16}N and ^{15}C decay events in the timing window of $[0.5, 25.0]$ s according to the analysis method described in Sec. III. In parallel, we also generated realistic MC simulations of both ^{16}N and ^{15}C whose fraction is fixed with the measured values described in Sec. III.

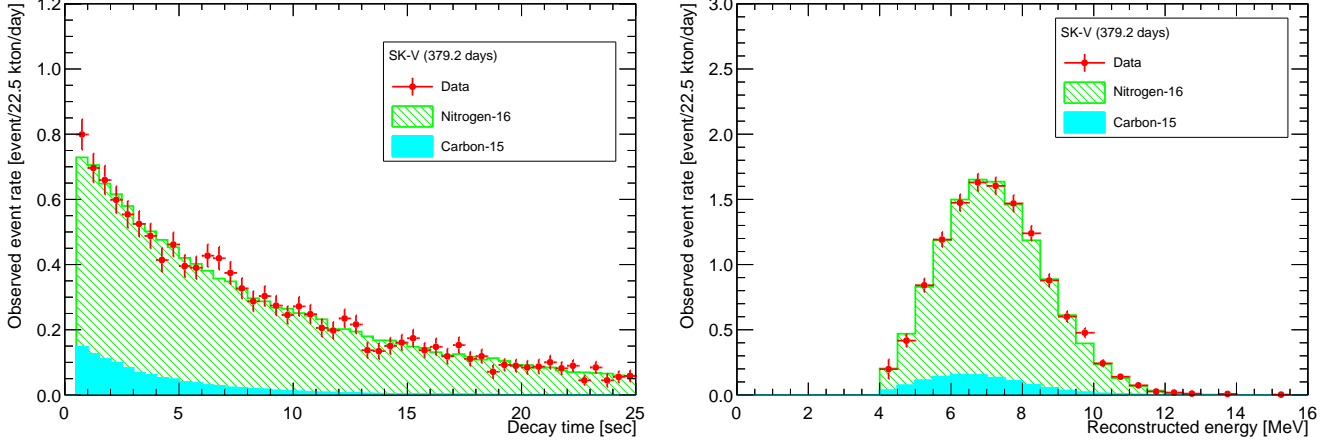


FIG. 21. Distributions of the time difference (left) in the timing window of $[0.5, 25.0]$ s and the reconstructed total energy (right) together with the best-fit of the components from ^{16}N and ^{15}C using the SK-V data. The definition of colors is the same as Fig. 14.

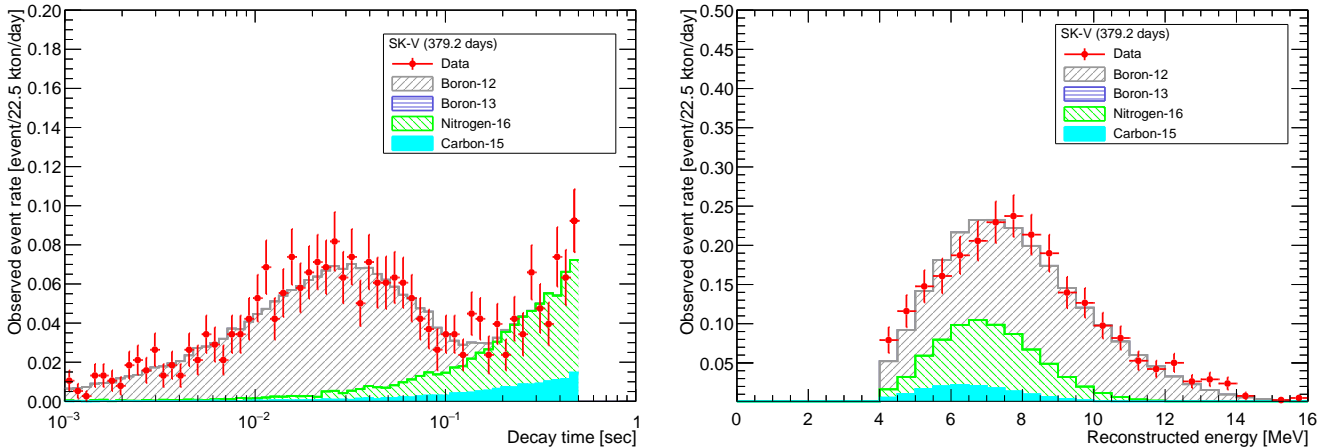


FIG. 22. Distributions of the time difference (left) in the timing window of $[0.001, 0.5]$ s and the reconstructed total energy (right) together with the best-fit of the components from ^{12}B , ^{13}B , ^{16}N , and ^{15}C using the SK-V data. The definition of colors is the same as Fig. 17. As shown in Fig. 16, the best-fit result of the SK-V demonstrates no component of ^{13}B decays in the analysis sample. As such, there is no contribution from ^{13}B decay in both panels.

For the evaluation of the energy scale, we used the effective hit parameter N_{eff} , which is defined as the number of PMT hits after applying a correction for the relative difference of PMT performance, the contributions of dark rate and late arrival hits, the effective surface area of PMTs, and light attenuation in the water [29].

Figure 25 shows the time variation of N_{eff} and compares the energy scale by the natural source sample with that evaluated by the DT calibration [63]. The energy scale is evaluated by the natural source sample and it was found that the estimated energy scale is stable within a $\pm 1\%$ level when we ignore the offset from the zero. This demonstrates that we can monitor the energy scale by using the natural source sample during the usual operation of the SK detector.

As detailed in Ref. [29], we carried out water convec-

tion throughout the SK detector by controlling the supply water temperature to achieve the uniformity of the water quality. During that period, the energy scale evaluated by the DT calibration is almost zero (right most point in the bottom panel of Fig. 25) and this demonstrates that the difference between the DT calibration data and the MC simulation in the SK-IV data sample can be explained by the incomplete modeling of the water properties. Although completeness exists in the MC simulation, the energy scale estimated by the DT calibration keeps within a $\pm 0.5\%$ level.

Due to low statistics of natural source samples, there exist larger uncertainties compared with those of DT calibration. But, we demonstrated the consistency of two calibration results within a $\pm 2\%$ level as shown in Fig. 25.

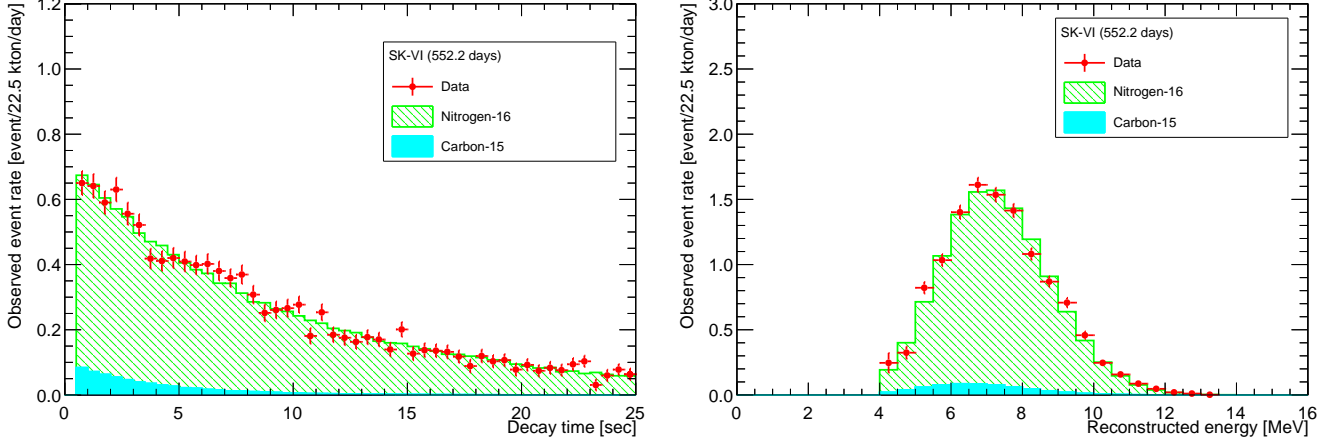


FIG. 23. Distributions of the time difference (left) in the timing window of $[0.5, 25.0]$ s and the reconstructed total energy (right) together with the best-fit of the components from ^{16}N and ^{15}C using the SK-VI data. The definition of colors is the same as Fig. 14.

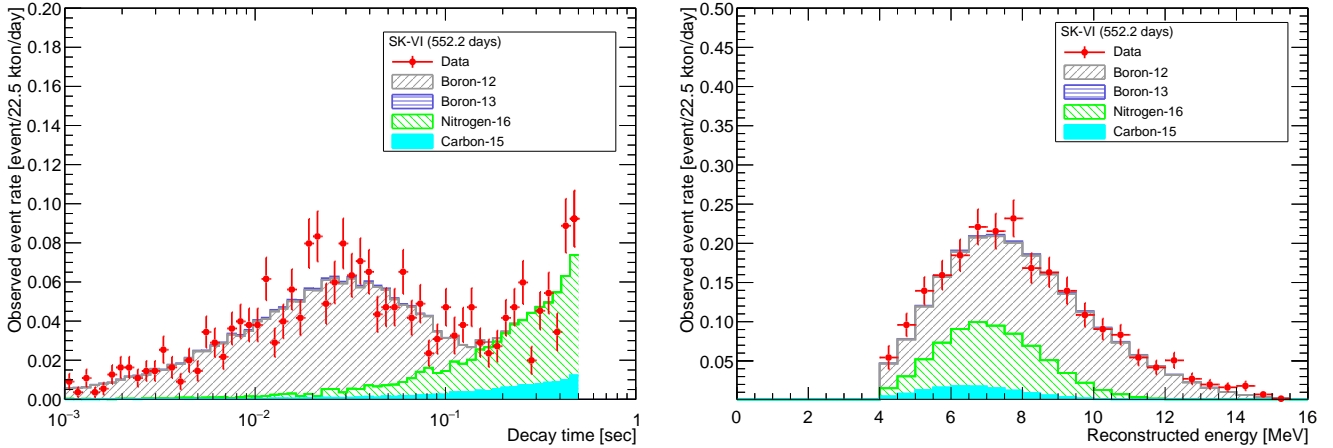


FIG. 24. Distributions of the time difference (left) in the timing window of $[0.001, 0.5]$ s and the reconstructed total energy (right) together with the best-fit of the components from ^{12}B , ^{13}B , ^{16}N , and ^{15}C using the SK-VI data. The definition of colors is the same as Fig. 17.

2. Position dependence of energy scale

In general, the solar neutrino interactions uniformly occur throughout the detector volume. The uniformity of the water pattern inside the SK detector affects the energy scale because the propagation of photons reflects the situation of absorption, reflection, and scattering in water. Hence, the position dependence of the energy scale is critical for the precise measurement of the solar neutrino spectrum in the SK detector. Figure 26 shows the position dependence of the energy scale. Although the statistical fluctuation can be seen, the natural source sample demonstrates the position dependence of the energy scale within a $\pm 2\%$ level and is consistent with that evaluated by the DT calibration source.

3. Directional dependence of energy scale

The direct test of matter effects on neutrino oscillations is the day/night cycle of solar neutrino interaction rates [92, 93]. The solar zenith angle of the scattered electron signal is used to approximate the neutrino travelling length through the Earth. To measure the day-night flux asymmetry of solar neutrinos in the SK detector, the directional dependence of the energy scale is important [94]. Figure 27 shows the directional dependence of the energy scale by natural source samples together with the DT calibration. As was seen for position dependence, the natural source sample also demonstrates the directional dependence of the energy scale within a $\pm 2\%$ level and is consistent with that evaluated by the DT calibration source.

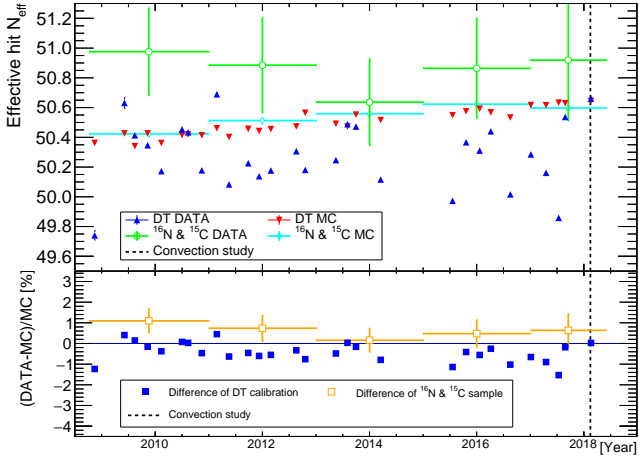


FIG. 25. Top panel: The energy scale using the effective hit N_{eff} as a function of time estimated by the ^{16}N sample as well as the DT calibration [29, 63] during the SK-IV period from 2008 to 2018. Due to low statistics, two years of natural source sample are merged into one dataset. Bottom panel: Their relative difference between the data and the MC simulations.

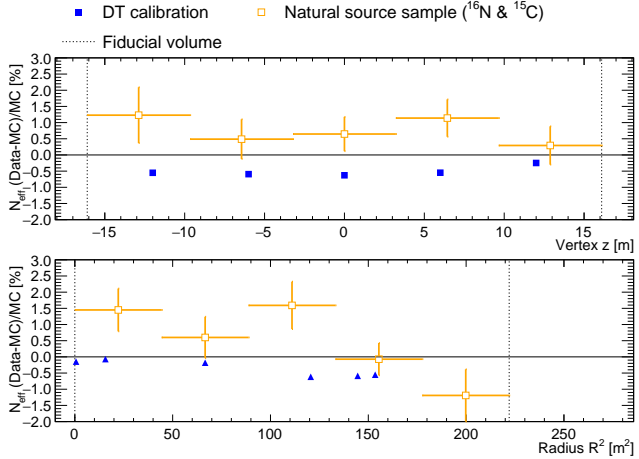


FIG. 26. The position dependence of the relative difference between the calibration data and the MC simulation by the natural source sample as well as the DT calibration [29, 63]. The top panel shows the position dependence on the vertex Z (height of the SK detector) and the bottom panel shows that on the detector's radius.

4. Summary of this section

As demonstrated in this article, naturally produced ^{16}N via negative muon capture on nuclei can statistically monitor the energy scale in the energy region of MeV during the usual operation of the detector even though

the production rate is low. Once the detector volume becomes larger, such as will be the case for the Hyper-Kamiokande detector [95], this analysis technique using

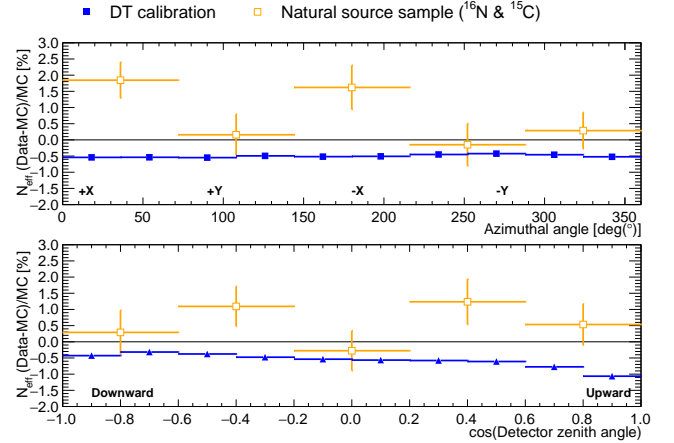


FIG. 27. The directional dependence of the relative difference between the calibration data and the MC simulation by the natural source sample as well as the DT calibration [29, 63]. The top panel shows the angular dependence on the azimuthal angle and the bottom panel shows that on the zenith angle. As mentioned in Ref. [29], the upward events are affected by the shadow due to the DT device above the target position. Hence, in the most upward bin ($0.8 < \cos \theta_{\text{Zenith}} < 1.0$) is noticeably reduced due to the actual shadow effect in the calibration data while such effect is not included in the MC simulation.

natural source samples is quite helpful for monitoring the energy scale in the MeV range during usual operation without calibration devices.

Appendix F: Correction of SK-I result

In the previous study [63], we explained that the production rate of ^{16}N is 11.9 ± 1.0 (stat. + syst.) event/11.5 kton/day by analyzing the SK-I data set assuming about 4% of the contamination of ^{15}C isotope decay events. This value corresponds to a ^{16}N production rate of 1.0 ± 0.1 event/kton/day. However, this value is completely different from that measured in this analysis, listed in Table XVI. This discrepancy happens because of the improper treatment of the selection efficiency of the stopping muon in the detector in the previous analysis. In fact, the selection efficiency of stopping muons in the previous analysis was estimated as 100%. Owing to this improper selection efficiency of stopping muon, we wrongly reported the low production rate of ^{16}N in the previous publication.

[1] R. Davis, Jr., D. S. Harmer, and K. C. Hoffman, Search for neutrinos from the sun, *Phys. Rev. Lett.* **20**, 1205 (1968).

[2] K. S. Hirata *et al.* (The Kamiokande-II collaboration), Observation of B-8 Solar Neutrinos in the Kamiokande-II Detector, *Phys. Rev. Lett.* **63**, 16 (1989).

[3] A. I. Abazov *et al.*, Search for neutrinos from sun using the reaction Ga-71 (electron-neutrino e-) Ge-71, *Phys. Rev. Lett.* **67**, 3332 (1991).

[4] P. Anselmann *et al.* (The GALLEX collaboration), Solar neutrinos observed by GALLEX at Gran Sasso., *Phys. Lett. B* **285**, 376 (1992).

[5] M. Altmann *et al.* (The GNO collaboration), GNO solar neutrino observations: Results for GNO I, *Phys. Lett. B* **490**, 16 (2000), arXiv:hep-ex/0006034.

[6] S. Fukuda *et al.* (The Super-Kamiokande collaboration), Solar B-8 and hep neutrino measurements from 1258 days of Super-Kamiokande data, *Phys. Rev. Lett.* **86**, 5651 (2001), arXiv:hep-ex/0103032.

[7] Q. R. Ahmad *et al.* (The SNO collaboration), Measurement of the rate of $\nu_e + d \rightarrow p + p + e^-$ interactions produced by ^8B solar neutrinos at the Sudbury Neutrino Observatory, *Phys. Rev. Lett.* **87**, 071301 (2001), arXiv:nucl-ex/0106015.

[8] Q. R. Ahmad *et al.* (The SNO collaboration), Direct evidence for neutrino flavor transformation from neutral current interactions in the Sudbury Neutrino Observatory, *Phys. Rev. Lett.* **89**, 011301 (2002), arXiv:nucl-ex/0204008.

[9] K. Eguchi *et al.* (The KamLAND collaboration), First results from KamLAND: Evidence for reactor anti-neutrino disappearance, *Phys. Rev. Lett.* **90**, 021802 (2003), arXiv:hep-ex/0212021.

[10] M. Agostini *et al.* (The Borexino collaboration), First Simultaneous Precision Spectroscopy of pp , ^7Be , and pep Solar Neutrinos with Borexino Phase-II, *Phys. Rev. D* **100**, 082004 (2019), arXiv:1707.09279 [hep-ex].

[11] M. Agostini *et al.* (The BOREXINO collaboration), Comprehensive measurement of pp -chain solar neutrinos, *Nature* **562**, 505 (2018).

[12] A. Gando *et al.* (The KamLAND collaboration), ^7Be Solar Neutrino Measurement with KamLAND, *Phys. Rev. C* **92**, 055808 (2015), arXiv:1405.6190 [hep-ex].

[13] D. Basilico *et al.* (The BOREXINO collaboration), Final results of Borexino on CNO solar neutrinos, *Phys. Rev. D* **108**, 102005 (2023), arXiv:2307.14636 [hep-ex].

[14] A. Allega *et al.* (The SNO+ collaboration), Measurement of the ^8B solar neutrino flux using the full SNO+ water phase dataset, *Phys. Rev. D* **110**, 122003 (2024), arXiv:2407.17595 [hep-ex].

[15] Z. Bo *et al.* (The PandaX collaboration), First Indication of Solar ^8B Neutrinos through Coherent Elastic Neutrino-Nucleus Scattering in PandaX-4T, *Phys. Rev. Lett.* **133**, 191001 (2024), arXiv:2407.10892 [hep-ex].

[16] E. Aprile *et al.* (The XENON collaboration), First Indication of Solar ^8B Neutrinos via Coherent Elastic Neutrino-Nucleus Scattering with XENO Nt , *Phys. Rev. Lett.* **133**, 191002 (2024), arXiv:2408.02877 [nucl-ex].

[17] S. P. Mikheyev *et al.*, Resonance Amplification of Oscillations in Matter and Spectroscopy of Solar Neutrinos, Sov. J. Nucl. Phys. **42**, 913 (1985).

[18] L. Wolfenstein, Neutrino Oscillations in Matter, *Phys. Rev. D* **17**, 2369 (1978).

[19] A. J. Baltz *et al.*, Effect of Transmission Through the Earth on Neutrino Oscillations, *Phys. Rev. D* **35**, 528 (1987).

[20] J. Bouchez *et al.*, Matter Effects for Solar Neutrino Oscillations, *Z. Phys. C* **32**, 499 (1986).

[21] E. D. Carlson, Terrestrially Enhanced Neutrino Oscillations, *Phys. Rev. D* **34**, 1454 (1986).

[22] M. Cribier *et al.*, MSW Regeneration of Solar ν_e in the Earth, *Phys. Lett. B* **182**, 89 (1986).

[23] S. T. Petcov, Diffractive - like (or parametric resonance - like?) enhancement of the earth (day - night) effect for solar neutrinos crossing the earth core, *Phys. Lett. B* **434**, 321 (1998), arXiv:hep-ph/9805262.

[24] P. Bakhti *et al.*, Oscillation tomography of the Earth with solar neutrinos and future experiments, *Phys. Rev. D* **101**, 123031 (2020), arXiv:2001.08030 [hep-ph].

[25] J. Hosaka *et al.* (The Super-Kamiokande collaboration), Solar neutrino measurements in super-Kamiokande-I, *Phys. Rev. D* **73**, 112001 (2006), arXiv:hep-ex/0508053.

[26] J. P. Cravens *et al.* (The Super-Kamiokande collaboration), Solar neutrino measurements in Super-Kamiokande-II, *Phys. Rev. D* **78**, 032002 (2008), arXiv:0803.4312 [hep-ex].

[27] K. Abe *et al.* (The Super-Kamiokande collaboration), Solar neutrino results in Super-Kamiokande-III, *Phys. Rev. D* **83**, 052010 (2011), arXiv:1010.0118 [hep-ex].

[28] K. Abe *et al.* (The Super-Kamiokande collaboration), Solar Neutrino Measurements in Super-Kamiokande-IV, *Phys. Rev. D* **94**, 052010 (2016), arXiv:1606.07538 [hep-ex].

[29] K. Abe *et al.* (The Super-Kamiokande collaboration), Solar neutrino measurements using the full data period of Super-Kamiokande-IV, *Phys. Rev. D* **109**, 092001 (2024), arXiv:2312.12907 [hep-ex].

[30] Y. Nakano *et al.*, Measurement of the radon concentration in purified water in the Super-Kamiokande IV detector, *Nucl. Instrum. Meth. A* **977**, 164297 (2020), arXiv:1910.03823 [physics.ins-det].

[31] Y. Zhang *et al.* (The Super-Kamiokande collaboration), First measurement of radioactive isotope production through cosmic-ray muon spallation in Super-Kamiokande IV, *Phys. Rev. D* **110**, 032003 (2024), arXiv:1509.08168 [hep-ex].

[32] S. Locke *et al.* (The Super-Kamiokande collaboration), New Methods and Simulations for Cosmogenic Induced Spallation Removal in Super-Kamiokande-IV, *Phys. Rev. D* **93**, 012004 (2016), arXiv:2112.00092 [hep-ex].

[33] R. Cohen, S. Devons, and A. Kanaris, Muon capture in oxygen, *Nuclear Physics* **57**, 255 (1964).

[34] T. W. Donnelly and J. D. Walecka, Semi-leptonic weak and electromagnetic interactions in nuclei with application to ^{16}O , *Phys. Lett. B* **41**, 275 (1972).

[35] F. Cannata, R. Graves, and H. Überall, The Capture of Muons by Complex Nuclei, *Riv. Nuovo Cim.* **7**, 133 (1977).

[36] K. Koshigiri, H. Ohtsubo, and M. Morita, Nuclear Structure Effects to Weak Nuclear Form-factors of $0+0-$ Transitions in $a = 16$ System, *Prog. Theor. Phys.* **62**, 706

(1979).

[37] I. S. Towner and F. C. Khanna, Role of 2p-2h states in weak $0+ - 0-$ transitions in $A = 16$ nuclei, *Nucl. Phys. A* **372**, 331 (1981).

[38] T. Marketin, N. Paar, T. Niksic, and D. Vretenar, Relativistic QRPA calculation of muon capture rates, *Phys. Rev. C* **79**, 054323 (2009), arXiv:0812.1947 [nucl-th].

[39] P. Guichon *et al.*, μ^- partial capture rates in ^{16}O , *Phys. Rev. C* **19**, 987 (1979).

[40] D. F. Measday, The nuclear physics of muon capture, *Phys. Rept.* **354**, 243 (2001).

[41] R. A. Eramzhian *et al.*, Towards a Better Understanding of O-16 Nuclear Structure: Muon Capture and Radiative Pion Capture Reactions, *Nucl. Phys. A* **190**, 294 (1977).

[42] B. Heisinger *et al.*, Production of selected cosmogenic radionuclides by muons: 2. Capture of negative muons, *Earth Planet. Sci. Lett.* **200**, 357 (2002).

[43] J. Allison *et al.*, Recent developments in Geant4, *Nucl. Instrum. Meth. A* **835**, 186 (2016).

[44] G. Battistoni *et al.*, Overview of the FLUKA code, *Annals Nucl. Energy* **82**, 10 (2015).

[45] T. Sato *et al.*, Particle and Heavy Ion Transport code System, PHITS, version 2.52, *J. Nucl. Sci. Technol.* **50**, 913 (2013).

[46] S. Abe and T. Sato, Implementation of muon interaction models in PHITS, *J. Nucl. Sci. Technol.* **54**, 101 (2017).

[47] O. Nairat, J. F. Beacom, and S. W. Li, Neutron tagging can greatly reduce spallation backgrounds in Super-Kamiokande, *Phys. Rev. D* **111**, 023014 (2025), arXiv:2409.10611 [hep-ph].

[48] Y. Fukuda *et al.* (The Super-Kamiokande collaboration), The Super-Kamiokande detector, *Nucl. Instrum. Meth. A* **501**, 418 (2003).

[49] K. Abe *et al.* (The Super-Kamiokande collaboration), Calibration of the Super-Kamiokande Detector, *Nucl. Instrum. Meth. A* **737**, 253 (2014), arXiv:1307.0162 [physics.ins-det].

[50] H. Kume *et al.*, 20-inch diameter photomultiplier, *Nucl. Instrum. Meth.* **205**, 443 (1983).

[51] K. Abe *et al.* (The Super-Kamiokande collaboration), First gadolinium loading to Super-Kamiokande, *Nucl. Instrum. Meth. A* **1027**, 166248 (2022), arXiv:2109.00360 [physics.ins-det].

[52] K. Abe *et al.* (The Super-Kamiokande collaboration), Second gadolinium loading to Super-Kamiokande, *Nucl. Instrum. Meth. A* **1065**, 169480 (2024), arXiv:2403.07796 [physics.ins-det].

[53] H. Nishino *et al.*, High-speed charge-to-time converter ASIC for the Super-Kamiokande detector, *Nucl. Instrum. Meth. A* **610**, 710 (2009), arXiv:0911.0986 [physics.ins-det].

[54] S. Yamada *et al.* (The Super-Kamiokande collaboration), Commissioning of the new electronics and online system for the Super-Kamiokande experiment, *IEEE Trans. Nucl. Sci.* **57**, 428 (2010).

[55] T. Tanimori *et al.*, Design and performance of semicustom analog IC including two tacs and two current integrators for 'Super-Kamiokande', *IEEE Trans. Nucl. Sci.* **36**, 497 (1989).

[56] H. Ikeda *et al.*, Monolithic shaper amplifier for multi-anode PMT readout, *Nucl. Instrum. Meth. A* **292**, 439 (1990).

[57] H. Zhang *et al.* (The Super-Kamiokande collaboration), Supernova Relic Neutrino Search with Neutron Tagging at Super-Kamiokande-IV, *Astropart. Phys.* **60**, 41 (2015), arXiv:1311.3738 [hep-ex].

[58] M. Shinoki *et al.* (The Super-Kamiokande collaboration), Measurement of the cosmogenic neutron yield in Super-Kamiokande with gadolinium loaded water, *Phys. Rev. D* **107**, 092009 (2023), arXiv:2212.10801 [hep-ex].

[59] H. Watanabe *et al.* (The Super-Kamiokande collaboration), First Study of Neutron Tagging with a Water Cherenkov Detector, *Astropart. Phys.* **31**, 320 (2009), arXiv:0811.0735 [hep-ex].

[60] K. Abe *et al.* (The Super-Kamiokande collaboration), Neutron tagging following atmospheric neutrino events in a water Cherenkov detector, *JINST* **17**, P10029, arXiv:2209.08609 [hep-ex].

[61] H. Kitagawa *et al.* (The Super-Kamiokande collaboration), Measurements of the charge ratio and polarization of cosmic-ray muons with the Super-Kamiokande detector, *Phys. Rev. D* **110**, 082008 (2024), arXiv:2403.08619 [hep-ex].

[62] M. Nakahata *et al.* (The Super-Kamiokande collaboration), Calibration of Super-Kamiokande using an electron linac, *Nucl. Instrum. Meth. A* **421**, 113 (1999), arXiv:hep-ex/9807027.

[63] E. Blaufuss *et al.* (The Super-Kamiokande collaboration), N-16 as a calibration source for Super-Kamiokande, *Nucl. Instrum. Meth. A* **458**, 638 (2001), arXiv:hep-ex/0005014.

[64] A. van der Schaaf *et al.*, Measurement of Neutron Energy Spectra and Neutron - γ Angular Correlations for the Muon Capture Process $^{16}\text{O}(\mu^-, \nu_\mu X n) ^{14}\text{N}, ^{15}\text{N}$, *Nucl. Phys. A* **408**, 573 (1983).

[65] L. Jokiniemi *et al.*, Muon capture on Li6, C12, and O16 from ab initio nuclear theory, *Phys. Rev. C* **109**, 065501 (2024), arXiv:2403.05776 [nucl-th].

[66] S. Miki *et al.* (The Super-Kamiokande collaboration), Neutron multiplicity measurement in muon capture on oxygen nuclei in the Gd-loaded Super-Kamiokande detector (2025), arXiv:2502.17002 [hep-ex].

[67] S. N. Kaplan *et al.*, Partial capture rates on muons by o-16 leading to excited nuclear states on n-15, *Phys. Rev. Lett.* **22**, 795 (1969).

[68] C. Galbiati *et al.*, Measuring the cosmic ray muon-induced fast neutron spectrum by (n,p) isotope production reactions in underground detectors, *Phys. Rev. C* **72**, 025807 (2005), [Erratum: Phys. Rev. C 73, 049906 (2006)], arXiv:hep-ph/0504227.

[69] S. W. Li *et al.*, First calculation of cosmic-ray muon spallation backgrounds for MeV astrophysical neutrino signals in Super-Kamiokande, *Phys. Rev. C* **89**, 045801 (2014), arXiv:1402.4687 [hep-ph].

[70] S. W. Li *et al.*, Spallation Backgrounds in Super-Kamiokande Are Made in Muon-Induced Showers, *Phys. Rev. D* **91**, 105005 (2015), arXiv:1503.04823 [hep-ph].

[71] S. W. Li *et al.*, Tagging Spallation Backgrounds with Showers in Water-Cherenkov Detectors, *Phys. Rev. D* **92**, 105033 (2015), arXiv:1508.05389 [physics.ins-det].

[72] S. Abe *et al.* (The KamLAND collaboration), Production of Radioactive Isotopes through Cosmic Muon Spallation in KamLAND, *Phys. Rev. C* **81**, 025807 (2010), arXiv:0907.0066 [hep-ex].

[73] G. Bellini *et al.* (The Borexino collaboration), Cosmogenic Backgrounds in Borexino at 3800 m water-equivalent depth, *JCAP* **08**, 049, arXiv:1304.7381 [physics.ins-det].

[74] Y. Abe *et al.* (The Double Chooz collaboration), Muon capture on light isotopes measured with the Double Chooz detector, Phys. Rev. C **93**, 054608 (2016), arXiv:1512.07562 [nucl-ex].

[75] S. Abe *et al.* (The KamLAND-Zen collaboration), Measurement of cosmic-ray muon spallation products in a xenon-loaded liquid scintillator with KamLAND, Phys. Rev. C **107**, 054612 (2023), arXiv:2301.09307 [hep-ex].

[76] A. Tang, G. Horton-Smith, V. A. Kudryavtsev, and A. Tonazzo, Muon simulations for Super-Kamiokande, KamLAND and CHOOZ, Phys. Rev. D **74**, 053007 (2006), arXiv:hep-ph/0604078.

[77] R. Brun, F. Bruyant, F. Carminati, S. Giani, M. Maire, A. McPherson, G. Patrick, and L. Urban, GEANT Detector Description and Simulation Tool (1994).

[78] S. Agostinelli *et al.* (The GEANT4 collaboration), Geant4 - A Simulation Toolkit, Nucl. Instrum. Meth. A **506**, 250 (2003).

[79] J. Allison *et al.*, Geant4 developments and applications, IEEE Trans. Nucl. Sci. **53**, 270 (2006).

[80] J. Quesada Molina *et al.*, Recent Developments in Pre-Equilibrium and De-Excitation Models in Geant4, Prog. Nucl. Sci. Technol. **2**, 936 (2011).

[81] National Nuclear Data Center, Brookhaven National Laboratory, Evaluated nuclear structure data file (n.d.), <https://www.nndc.bnl.gov/ensdf/>.

[82] S. Desai, *High energy neutrino astrophysics with Super-Kamiokande*, Ph.D. thesis, Boston university (2004).

[83] Z. Conner, *A study of solar neutrinos using the Super-Kamiokande detector*, Ph.D. thesis, University of Maryland (1997).

[84] M. Smy, Low Energy Event Reconstruction and Selection in Super-Kamiokande-III, in *30th International Cosmic Ray Conference* (2007).

[85] T. Wester *et al.* (The Super-Kamiokande collaboration), Atmospheric neutrino oscillation analysis with neutron tagging and an expanded fiducial volume in Super-Kamiokande I–V, Phys. Rev. D **109**, 072014 (2024), arXiv:2311.05105 [hep-ex].

[86] H. Daniel, Coulomb capture of muons and atomic radius, Z. Phys. A **291**, 29 (1979).

[87] J. Meijs, T. B. Coplen, M. Berglund, W. A. Brand, P. De Bièvre, M. Gröning, N. E. Holden, J. Irrgeher, R. D. Loss, T. Walczyk, *et al.*, Isotopic compositions of the elements 2013 (iupac technical report), Pure and Applied Chemistry **88**, 293 (2016).

[88] T. Suzuki *et al.*, Total Nuclear Capture Rates for Negative Muons, Phys. Rev. C **35**, 2212 (1987).

[89] F. R. Kane *et al.*, Muon capture rates on ^{16}O leading to bound states of ^{16}N , Phys. Lett. B **45**, 292 (1973).

[90] J. S. O' Connell, T. W. Donnelly, and J. D. Walecka, Semileptonic weak interactions with C^{12} , Phys. Rev. C **6**, 719 (1972).

[91] M. R. Dragowsky *et al.*, The N-16 calibration source for the Sudbury Neutrino Observatory, Nucl. Instrum. Meth. A **481**, 284 (2002), arXiv:nucl-ex/0109011.

[92] M. B. Smy *et al.* (The Super-Kamiokande collaboration), Precise measurement of the solar neutrino day/night and seasonal variation in Super-Kamiokande-1, Phys. Rev. D **69**, 011104 (2004), arXiv:hep-ex/0309011.

[93] G. Bellini *et al.* (The Borexino collaboration), Absence of day–night asymmetry of 862 keV ^{7}Be solar neutrino rate in Borexino and MSW oscillation parameters, Phys. Lett. B **707**, 22 (2012), arXiv:1104.2150 [hep-ex].

[94] A. Renshaw *et al.* (The Super-Kamiokande collaboration), First Indication of Terrestrial Matter Effects on Solar Neutrino Oscillation, Phys. Rev. Lett. **112**, 091805 (2014), arXiv:1312.5176 [hep-ex].

[95] K. Abe *et al.* (The Hyper-Kamiokande proto-collaboration), Hyper-Kamiokande Design Report (2018), arXiv:1805.04163 [physics.ins-det].